Pervanadate-induced oxidation relieves autoinhibition of SRC protein tyrosine kinase

Katie E. Mulholland[1], Maxime Bourguet[2], Nuo Cheng[3], Oisharja Rahman[1], Daria Ezeriņa[4,5,6], Leonard A. Daly[7], Tiffany Lai[1], Silvia Aldaz Casanova[1], Pau Creixell[3], Claire E. Eyers[7], Joris Messens[4,5,6], Patrick A. Eyers[8], Dominic P. Byrne[8*], Hayley J. Sharpe[1*].

Affiliations:

[1] Signalling Programme, Babraham Institute; Cambridge, UK

[2] MRC Laboratory of Molecular Biology; Cambridge, UK

[3] CRUK Cambridge Institute; Cambridge, UK

[4] VIB-VUB Center for Structural Biology, Vlaams Instituut Voor Biotechnologie; Brussels, Belgium

[5] Brussels Center for Redox Biology, Vrije Universiteit Brussel; Brussels, Belgium

[6] Structural Biology Brussels, Vrije Universiteit Brussel; Brussels, Belgium

[7] Centre for Proteome Research, Institute of Systems, Molecular and Integrative Biology, University of Liverpool; Liverpool, UK.

[8] Department of Biochemistry, Cell and Systems Biology, Institute of Systems, Molecular and Integrative Biology, University of Liverpool; Liverpool, UK.

*Corresponding authors. Email: hayley.sharpe@babraham.ac.uk and d.byrne@liverpool.ac.uk.

One sentence summary

The widely used PTP inhibitor pervanadate perturbs cellular redox homeostasis and directly activates SRC to promote high level of phosphotyrosine.

Abstract

Dynamic regulation of protein tyrosine phosphorylation (pTyr) by phosphatases (PTPs) and kinases enables cells to sense and respond to environmental changes. The widely used chemical probe Pervanadate (PV) induces accumulation of high levels of pTyr in cells, an effect primarily attributed to its properties as a PTP inhibitor. This led to the assertion that PTPs are the master gatekeeper of intracellular pTyr homeostasis. Here, we use diverse approaches to reveal that PV disrupts cellular redox homeostasis and directly activates SRC family tyrosine kinases *via* oxidation of specific cysteine residues. Using mass spectrometry and biophysical approaches, we show that oxidation activates SRC by disrupting autoinhibition and altering phosphopeptide binding by its SH2 domain. We further establish that redox-sensitive cysteine residues are essential for SRC to promote cellular overgrowth. Our findings call for a re-evaluation of PV-based experiments and provide compelling evidence that oxidation is a crucial mechanism in controlling the oncogenic properties of SRC.

Introduction

Phosphorylation of protein tyrosine residues (pTyr) is a critical posttranslational modification that orchestrates diverse cellular processes (*1*) and is often dysregulated in disease (*2, 3*). Dynamic pTyr levels are controlled by the activities of protein tyrosine phosphatases (PTPs) and kinases (PTKs). Disruption of both PTPs and PTKs can lead to pathological conditions, highlighting the importance of understanding their regulation in homeostasis and disease. The development of specific PTP inhibitors has been challenging, with only a few compounds advancing to clinical trials (*4, 5*). As a result, generic PTP inhibitors remain invaluable in gaining insight into pTyr functions and regulation. Of these, orthovanadate (OV), commonly added to cell lysis buffers, and pervanadate (PV), are important tools (*6*). OV acts as a phosphate mimetic that competitively inhibits PTPs, while PV is produced by combining hydrogen peroxide (H_2O_2) with OV, followed by the addition of catalase to remove excess H_2O_2 (**Fig. 1A**) (*6, 7*).

PV exists in multiple oxidation states, containing up to three peroxogroups (*8, 9*). In cells, PV treatment rapidly elevates pTyr levels, enabling PTP substrates to be analyzed through 'trapping' and dephosphorylation approaches (*10*). PV is established to inhibit PTPs by hyperoxidizing the low pKa catalytic cysteine to sulfonic acid (*11*). Due to the structural similarity between phosphate and vanadate, it has been proposed that PV exhibits high affinity for the PTP active site (*6*), leading to the conclusion that its effects are predominantly driven through PTP inhibition (*12*). Moreover, the capacity of PV to reproduce key cellular activation states has fostered the prevailing view that PTPs are constitutively active, constantly removing pTyr from proteins (*13*). Furthermore, this concept is a key pillar in the kinetic segregation model, which proposes that steric exclusion of the highly abundant receptor PTP, CD45, is sufficient to trigger T cell activation (*14*), based on experiments showing that PV mimics T cell activation (*15, 16*).

Cellular effects of PV are often indirectly linked to PTK activation, since PTPs are assumed to suppress activity (*12*). However, PTP function is more complex, with several PTPs, including CD45, preventing autoinhibition of PTKs via inhibitory phosphosites (*17, 18*). Furthermore, the catalytic activities of certain PTKs, including EGFR and SRC, are enhanced following reversible oxidation of conserved regulatory cysteine residues (*19-24*). Given that PV possesses peroxo groups with oxidizing potential, we hypothesized that its cellular effects on pTyr levels might extend beyond PTP inhibition to include direct oxidation of redox-sensitive cysteines in other proteins (*25, 26*), including PTKs. Here, we show that the SFKs SRC and YES1 are directly activated by PV. Using conformational analysis and biophysical approaches, we have determined the mechanisms by which PV-induced oxidation relieves SRC autoinhibition. Additionally, we identified a key role for redox-active cysteines in SRC-regulated cell growth and control of Hippo signaling. Our study defines redox-based mechanisms for SRC activation and highlights the importance of cysteine oxidation in oncogenic transformation. In addition, our data call for a mechanistic reinterpretation of the effects of pervanadate on phosphotyrosine and redox proteomes.

Results

Figure 1

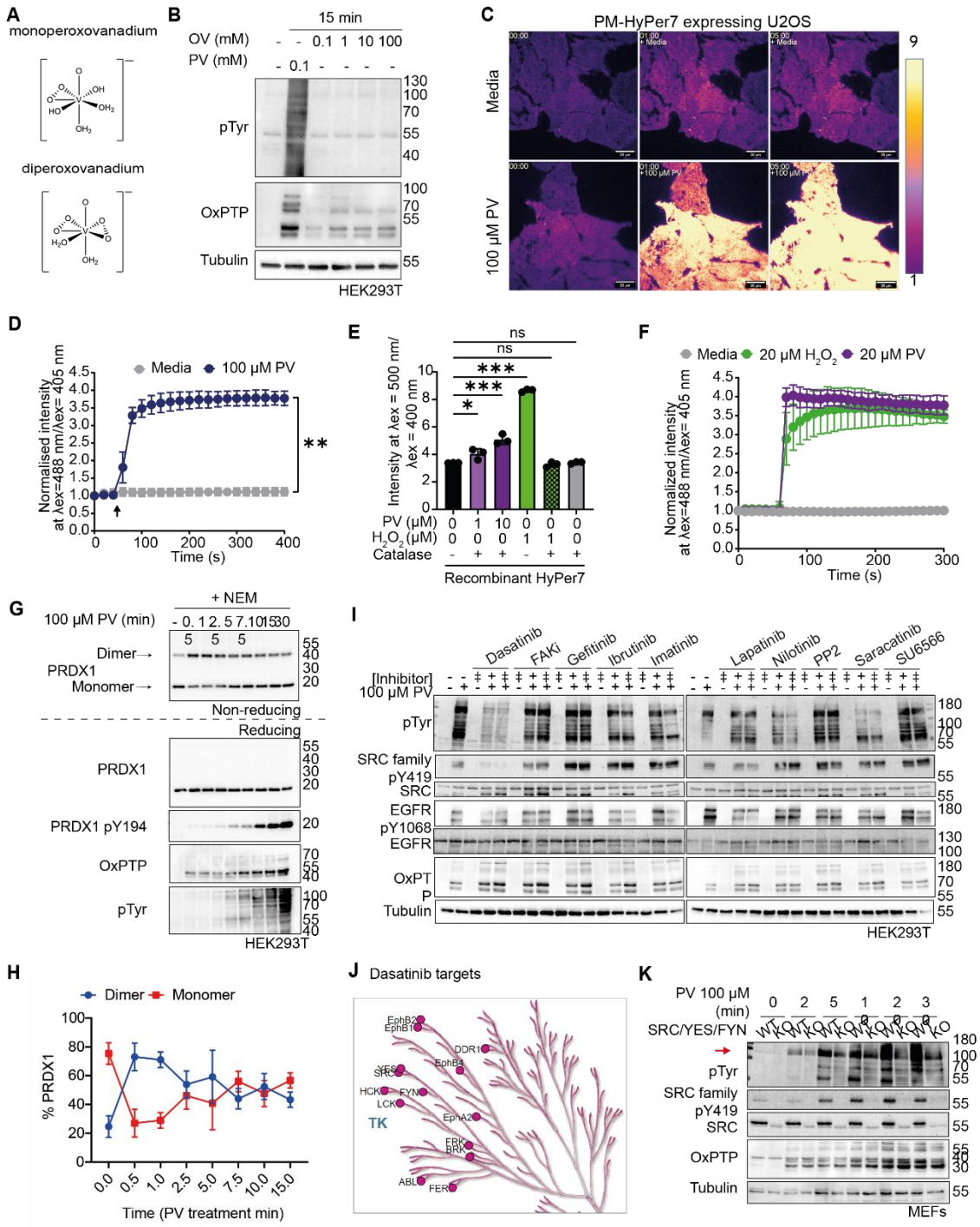

Fig. 1. PV perturbs redox homeostasis and induces tyrosine phosphorylation in SRC dependent manner.

(A) Schematic of mono-peroxo and di-peroxo-vanadium (PV compounds) generated using ChemDraw. **(B)** HEK293T cells were treated as shown, lysed and subjected to immunoblot analysis using the indicated antibodies. Image representative of N=3 experiments. (**C**) Representative false colour images of F488/405 ratio (scaled 1-9) from **movies S1 and S2** of U2OS cells stably expressing plasma membrane (PM) localised HyPer7 and treated with 100

97 μM PV or media. Scale bar = 20 μm. (**D**) Quantification of the ratio of the two excitation maxima
98 (F488/405), normalized against initial value, of PM-HyPer7 expressing U2OS cells over a time
99 course, imaged every 20 s. Treatments were added at 60 s (arrow). Mean of n=3 ± SD plotted.
100 ** $p \leq 0.001$ Unpaired t-test at t= 400 s. (**E**) Ratio of the two excitation maxima (F500/400) of
101 recombinantly expressed HyPer7 (2.5 μM) following its treatment with the indicated reagents.
102 The bars represent the mean of n=3 ± SD. *** $p \leq 0.001$; ns – non-significant. The p-value is
103 based on Dunnett's multiple comparisons test of a one-way ANOVA. (**F**) Quantification of the
104 ratio of the two excitation maxima (F488/405), normalized against initial value, of PM-HyPer7
105 expressing U2OS cells over a time course, imaged every 20 s. Treatments were added at 60
106 s (arrow). Mean of n=3 ± SD plotted. (**G**) Cells were subjected to the indicated PV time course,
107 washed with PBS with catalase and NEM, prior to lysis without NEM. Samples were resolved
108 on non-reducing or reducing gels as indicated to distinguish PRDX1 monomers from disulfide-
109 linked dimers. Total and phospho PRDX1 blots are from separate gels but the same samples.
110 Representative of n=3 experiments. (**H**) Densitometric quantification of PRDX1 dimer and
111 monomer bands from G. Mean of n=3 ± SD plotted. (**I**) HEK293T cells were treated with the
112 indicated tyrosine kinase inhibitors at IC_{50} (+) and 2.5x IC_{50} (‡) concentrations for 2 h prior to
113 addition of 100 μM PV for 15 min before lysis and immunoblotting with annotated antibodies.
114 (**J**) Dasatinib targets based on (*71*) and mapped onto the tyrosine kinase arm of the Human
115 kinome using kinmap (http://kinhub.org/kinmap/). (**K**) WT and Src/Yes/Fyn (SYF) WT and KO
116 cells were stimulated with 100 μM PV for the indicated times prior to lysis and immunoblotting
117 with indicated antibodies. Red arrow indicates 130 kDa. Representative of 3 experiments.
118
119 See also Figs. S1-S3.
120

121 **Pervanadate promotes cysteine thiol oxidation**
122 We initially set out to characterize cellular effects of the PTP inhibitors PV and OV. As
123 expected, PV induced a rapid pTyr accumulation in HEK293T cells with concomitant
124 irreversible PTP oxidation (OxPTP) (**Fig. 1B**). In contrast, the PTP inhibitor OV had minimal
125 effect on global pTyr despite the induction of irreversible PTP oxidation at higher doses (**Fig.**
126 **1B**). Longer treatment (4h) with high doses of OV, resulted in more pronounced upregulation
127 of pTyr and PTP hyperoxidation, consistent with previous reports of oxidative damage by OV
128 (*27*) (**Fig. S1A**). We next asked whether our OV preparations inhibit PTPs. First, we confirmed
129 that OV inhibits the phosphatase activity of recombinant purified PTPRK *in vitro*, albeit less
130 potently than PV (**Figs. S1B-S1C**), aligning with previous reports (*28*). Furthermore, Flag-
131 PTPRK immunoprecipitated from OV or PV treated cells was catalytically inactive (**Figs. S1D-**
132 **S1E**). Importantly, and in contrast to PV, OV did not induce extensive tyrosine phosphorylation
133 at this concentration (**Figs. S1F-S1G**). Collectively these data suggest that PTP inhibition
134 alone is necessary, but not sufficient, for high-level global induction of pTyr. We next explored
135 the possibility that PV could have functions beyond PTP inhibition that promote
136 supraphysiological levels of pTyr accumulation.
137
138 Since the pTyr-inducing function of PV is usually attributed to PTP oxidation, we investigated
139 whether it has broader oxidizing activities in cells. To this end, we used HyPer7, a ratiometric
140 biosensor that is oxidized by peroxides and reduced by thioredoxins and reduced glutathione
141 (GSH) within cells (*29-31*). Treating U2OS cells expressing myristoylated, plasma membrane-
142 anchored HyPer7 with 100 μM PV led to rapid biosensor oxidation compared to media-treated
143 cells (**Figs. 1C-1D and movies S1-S2**). In contrast, treatment of cells with 50-500 fold higher
144 levels of OV decreased the ratio of oxidized:reduced HyPer7 compared to media alone (**Fig.**
145 **S1H**). *In vitro*, PV directly oxidized purified recombinant HyPer7, although far less potently
146 than H_2O_2 (**Fig. 1E**). By comparison, both 20 μM PV and H_2O_2 rapidly oxidized HyPer7 in cells
147 equivalently (**Fig. 1F**). Thus, despite lower direct reactivity with HyPer7, PV is as effective as
148 H_2O_2 (at 20 μM) at inducing HyPer7 oxidation in cells. This indicates that PV elicits its effects
149 on HyPer7 in cells by perturbing antioxidant pathways, such as the thioredoxin pathway.
150
151 We next performed a time course of PV treatment and monitored the oxidation state of
152 peroxiredoxin 1 (PRDX1), an endogenous substrate of the thioredoxin pathway. Upon
153 oxidation by H_2O_2, PRDX forms disulfide-linked dimers, which are detectable as slower
154 migrating species after non-reducing SDS-PAGE. To block post-lysis oxidation, samples were
155 treated with catalase and N-ethyl maleimide (NEM). Within 30s, PV increased PRDX1
156 disulfide-linked dimers that were undetectable under reducing conditions (**Figs. 1G, 1H and**
157 **S1I**). We also detected a time dependent increase in PRDX1 phosphorylation (pY194), which
158 is associated with impaired PRDX catalytic function (*32*). Together these data suggest that PV
159 fundamentally perturbs redox homeostasis. Strikingly, PTPs were irreversibly oxidized 30 s
160 post PV treatment, several minutes before the peak in global tyrosine phosphorylation is
161 evident, suggesting sustained or induced PTK activity. Since several kinases also possess
162 redox-active cysteines (*19-24*), we next focused on the role of PTKs in driving the PV pTyr
163 response.
164
165 **PV-induced pTyr depends on specific PTKs, including SRC**
166 To determine which PTKs might contribute to PV-induced increases in pTyr, we took an
167 unbiased approach pre-treating cells with a panel of pharmacological PTK inhibitors. PV was
168 equally effective at oxidizing PTPs in cells treated with the inhibitors but dasatinib and

169 saracatanib profoundly limited PV-induced pTyr levels (**Figs. 1I and S2**). Dasatinib and
170 saracatanib inhibit SFKs, ABL and EPH kinases (**Fig. 1J**). SRC activation has previously been
171 linked to PV-induced pTyr signaling (*12, 33*), so we employed genetic manipulation to validate
172 the role of SFKs in this process. We observed an attenuated pTyr response when treating
173 Src/Yes/Fyn knockout (KO) MEFs compared to WT cells when treated with 100 μM PV,
174 despite equivalent levels of PTP oxidation (**Fig. 1K**). We also detected increased Abl1
175 expression in KO MEFs (**Fig. S3A**), which could explain the hyperphosphorylated protein band
176 at ~130 kDa induced by PV (**Fig. 1K, red arrow**). However, knockdown of Abl1 in SYF KO
177 MEFs did not further attenuate the PV response or affect the intensity of the 130 kDa band
178 (**Fig. S3B**). Knocking out SRC in HAP1 cells also decreased the levels of pTyr induced in
179 response to PV (**Fig. S3C**). Additionally, knockdown of SRC and YES1, but not FGR, in
180 HEK293T cells led to reduced PV stimulated pTyr (**Fig. S3D**). Thus, SFKs are key mediators
181 of the cellular PV response.
182

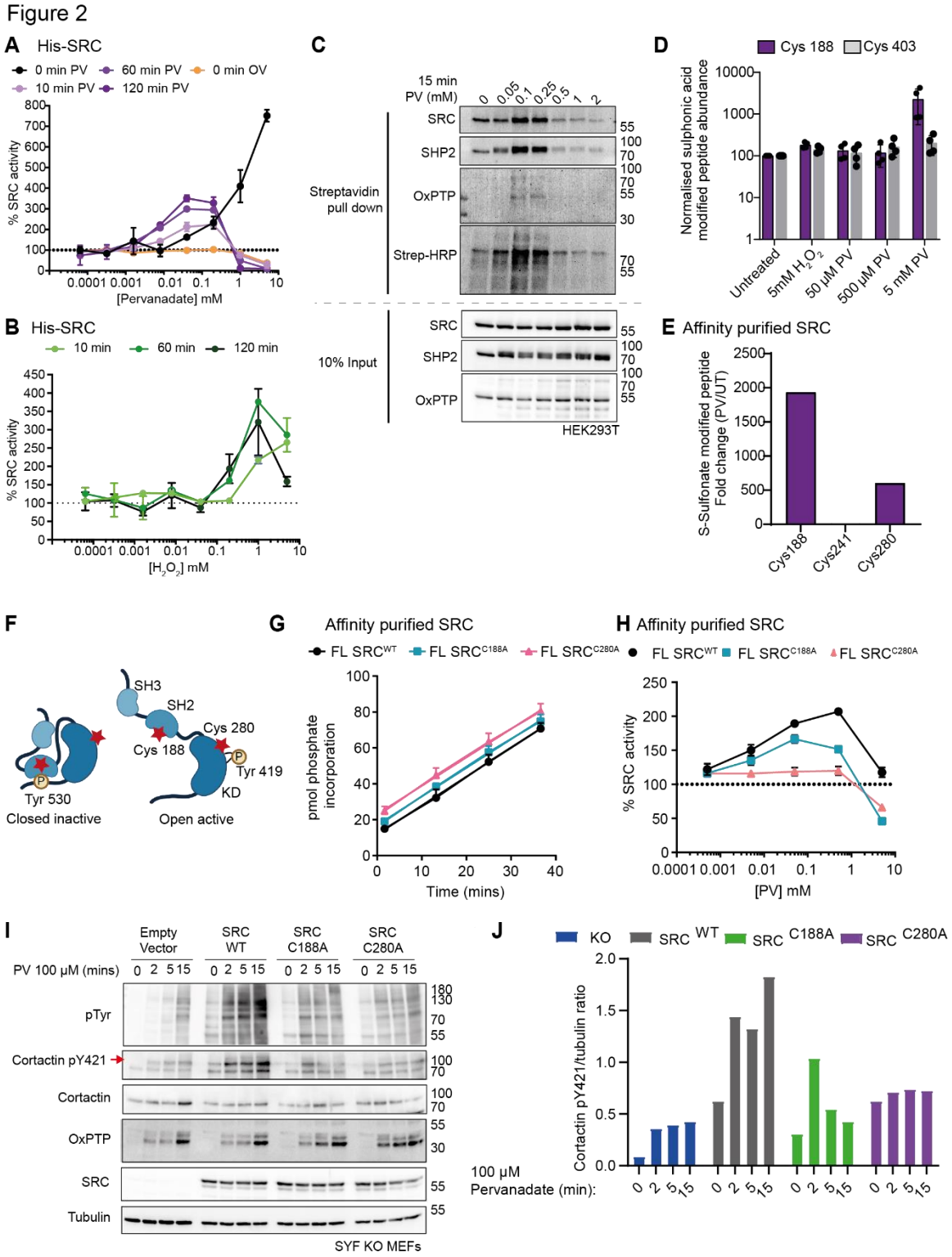

Fig. 2. SRC is oxidized on specific cysteines and activated by PV.
(**A**) 6xHis-SRC (3 ng) dependent phosphorylation of a specific fluorescent substrate (2 µM). Data shown is relative SRC activity in the presence of the indicated concentrations of PV compared to a buffer only control. SRC was preincubated for 0, 10, 60 or 120 mins prior to initiation of the kinase assay. Means ± SD n=3 experiments are shown. (**B**) Dose response curve for H_2O_2 pre-incubated with recombinant 6xHis-SRC (3 ng) for the indicated time periods. Reactions were initiated with the addition of peptide substrate and ATP, and

192 phosphorylation was measured after 15- and 25-mins assay time. Data shown is relative SRC
193 activity in the presence of the indicated concentrations of H_2O_2 compared to a buffer only
194 control. Means of n=3 ± SD shown. (**C**) HEK293T cells treated with the indicated
195 concentrations of PV for 15 min, were lysed in catalase and NEM-containing buffer. Reversibly
196 oxidised thiols were reduced with TCEP, and newly regenerated thiol(ate)s were labelled with
197 Iodoacetyl-PEG2-Biotin. Lysates and biotinylated proteins were then affinity purified using
198 streptavidin beads and subjected to immunoblotting with indicated antibodies. Blot
199 representative of 3 experiments. (**D**) HEK293T cells transiently expressing StrepII-tag fused
200 SRC were treated as indicated, and SRC affinity purified by streptactin pull down. Purified
201 protein was then subjected to tryptic digest and analysed by LC/MS-MS for triply oxidised
202 cysteine (sulphonic acid). (**E**) SRC isolated from transfected HEK293T cells by streptactin
203 affinity purification was incubated with or without 5 mM PV, followed by tryptic digest and
204 analysis by LC MS/MS. Values are normalized against abundance of non-cysteine containing
205 SRC peptides. (**F**) Schematic of SRC kinase indicating the position of two key regulatory
206 phosphosites (Circle with P) as well as the two most readily oxidixed cysteine residues (red
207 stars). (**G**) Surface electrostatic potential (*72*) for regions surrounding Cys 280 (PDB:2SRC)
208 and Cys 188 and Cys241 (PDB:1Y57). Units = K_bT/e_c. (**H**) Phosphorylation of the fluorescent
209 peptide substrate by WT (black), C188A (blue) and C280A (red) SRC isolated from HEK293T
210 cells by streptactin affinity purification was measured after 30 min. Means of n=3 ± SD are
211 shown. (**I**) Dose-response curves for PV. WT (black), C188A (blue) and C280A (red) SRC
212 isolated from HEK-293T cells by streptactin affinity purification and incubated with the
213 indicated concentrations of PV for 10 mins. Phosphorylation of the fluorescent peptide
214 substrate was measured after 15 min. Data shown is % SRC activity compared to a buffer
215 control. Means of n=3 ±SD are shown. FL = full-length. (**J**) SYF KO MEFs were retrovirally-
216 transduced with specified SRC expression constructs and treated with PV as shown, before
217 lysis and immunoblotting with indicated antibodies. Red arrow indicates relevant band.
218 Representative of >3 experiments. (**K**) Densitometric quantification of western blot in Fig. 2J.
219 Ratios of phosphorylated cortactin/total tubulin levels are shown.
220
221 See also Fig. S3.
222

223 **Pervanadate activates SRC via cysteine oxidation *in vitro* and in cells**
224 We hypothesized that PV induces potent pTyr accumulation in cells by directly activating
225 SFKs. We focused our initial experiments on SRC since its redox sensing via specific
226 cysteines is the best characterised amongst SFKs (*20*). Using purified recombinant SRC, we
227 determined that PV dose-dependently increased SRC kinase activity *in vitro* (**Fig. 2A**).
228 Introducing a pre-incubation period increased activation at lower PV concentrations but
229 decreased catalytic activity at higher PV concentrations (**Figs. 2A and S3E**). OV treatment
230 had no effect on SRC activation (**Fig. 2A**). Similar activity profiles have been reported for SRC
231 and EGFR in cells treated with H_2O_2 (*21, 22*), where higher peroxide concentrations were
232 inhibitory potentially due to oxidation of additional cysteines. In support of a redox mechanism,
233 we also observed H_2O_2 stimulation of SRC activity, but only at higher concentrations than PV
234 (**Figs. 2B and S3E**). To test whether PV induces cellular SRC oxidation, we used differential
235 alkylation to reveal TCEP-reversible thiol modifications by biotin labelling. At 0-250 μM PV,
236 SRC and the PTP SHP2 were increasingly enriched by streptavidin, indicating increased
237 reversible oxidation (**Fig. 2C**). Higher PV concentrations decreased streptavidin-enrichment
238 of both proteins, suggesting thiols had either become reduced, or irreversibly oxidized and
239 therefore resistant to reduction and alkylation. In fact, numerous biotinylated, reversibly
240 oxidized, proteins showed this trend. Additionally, we observed oxidation of both SRC and
241 SHP2 in the absence of PV, indicating a basal level of oxidative signaling in HEK293T cells,
242 consistent with the presence of PRDX1 dimers in untreated cells (**Fig. 1G**). Together, these
243 data demonstrate reversible oxidation of SRC by PV in cells.
244
245 To gain insight into the molecular mechanism(s) of SRC oxidation, we used a targeted
246 approach to identify cysteines oxidized by PV. At high PV concentrations, SRC cysteine thiols
247 appeared to be hyperoxidized to sulfinic or sulfonic acid (**Fig. 2C**), which are identifiable by
248 mass spectrometry (MS) without the need for differential alkylation. We therefore stimulated
249 cells overexpressing SRC with 5 mM PV for 30 min and analyzed affinity purified protein by
250 MS (**Fig. 2D and Table S1**). Peptides containing Cys 188 and Cys 403 were identified,
251 however, only Cys 188 showed a large increase in sulfonic acid modification following PV
252 treatment. We next analyzed purified, untagged SRC treated with PV, which identified sulfonic
253 acid modification of cysteines 188, 280 and 241 (**Fig. 2E and Table S2**). SRC Cys 241 was
254 less sensitive to hyperoxidation by PV than Cys 188 and Cys 280 (**Fig. 2E**), indicating distinct
255 accessibility or reactivity of individual cysteines (*34*). SRC comprises N-terminal, SRC
256 homology (SH)3, SH2 and kinase domains (**Fig. 2F**). Cys 188 is located within the SH2
257 domain pTyr binding pocket and is unique to SRC amongst SFKs, whilst Cys 280 resides in
258 the kinase domain P-loop of SRC, YES1 and FGR (**Figs. 2F and S3F**). Both Cys 280 and Cys
259 188 are found close to or within positively charged pockets on the surface of SRC (**Fig. 2G**).
260 In contrast, Cys 241, which was not oxidized by PV, is surface exposed in an electrostatically
261 neutral region of the SH2 domain (**Fig. 2G**). Together this reveals selective oxidation of Cys
262 188 and 280 by PV.
263
264 The conservation of Cys 280 in SFKs prompted us to also evaluate sensitivity of YES1 activity
265 to oxidation, especially given its role in the PV response in cells (**Fig. S3D**). Like SRC, PV
266 dose dependently increased YES1 activity (**Fig. S3G**). In contrast, H_2O_2 had a negligible
267 impact on activity (**Fig. S3H**), indicating differences in sensitivity to each oxidant. To directly
268 assess the impact of Cys 188 and Cys 280 on SRC kinase activity *in vitro*, we affinity purified
269 untagged WT (SRC^{WT}) and mutant (SRC^{C188A} and SRC^{C280A}) forms. All three proteins
270 displayed equivalent kinase activity (**Fig. 2H**). However, when treated with PV, a dose-

271 dependent increase in SRC^{WT} activity was evident, which was absent for SRC^{C280A} and
272 impaired for SRC^{C188A} (**Fig. 2I**). At higher PV concentrations, all proteins were inhibited,
273 potentially indicating oxidation of additional cysteines. Thus, PV-induced SRC activation
274 requires Cys 188 and Cys 280.
275
276 We next asked whether these cysteine residues are important for the cellular pTyr response
277 to PV. To this end, we introduced chicken Src and mutants equivalent to C188A and C280A
278 into SYF KO MEFs. Human SRC residue numbering is used hereafter for clarity and
279 consistency. In response to PV, reintroduction of SRC^{WT} increased global pTyr levels and
280 phosphorylation of the SRC substrate cortactin, however, this was impaired for SRC^{C188A} and
281 SRC^{C280A} indicating a role for these cysteines in driving signaling in response to PV (**Figs. 2J**
282 **and 2K**). Importantly, PTP catalytic cysteine hyperoxidation detected by oxPTP was
283 comparable in all cell lines. Together, our data suggest that oxidation of Cys 188 and 280 by
284 PV are important for activating SRC and driving cellular increases in pTyr-containing
285 substrates.

Figure 3

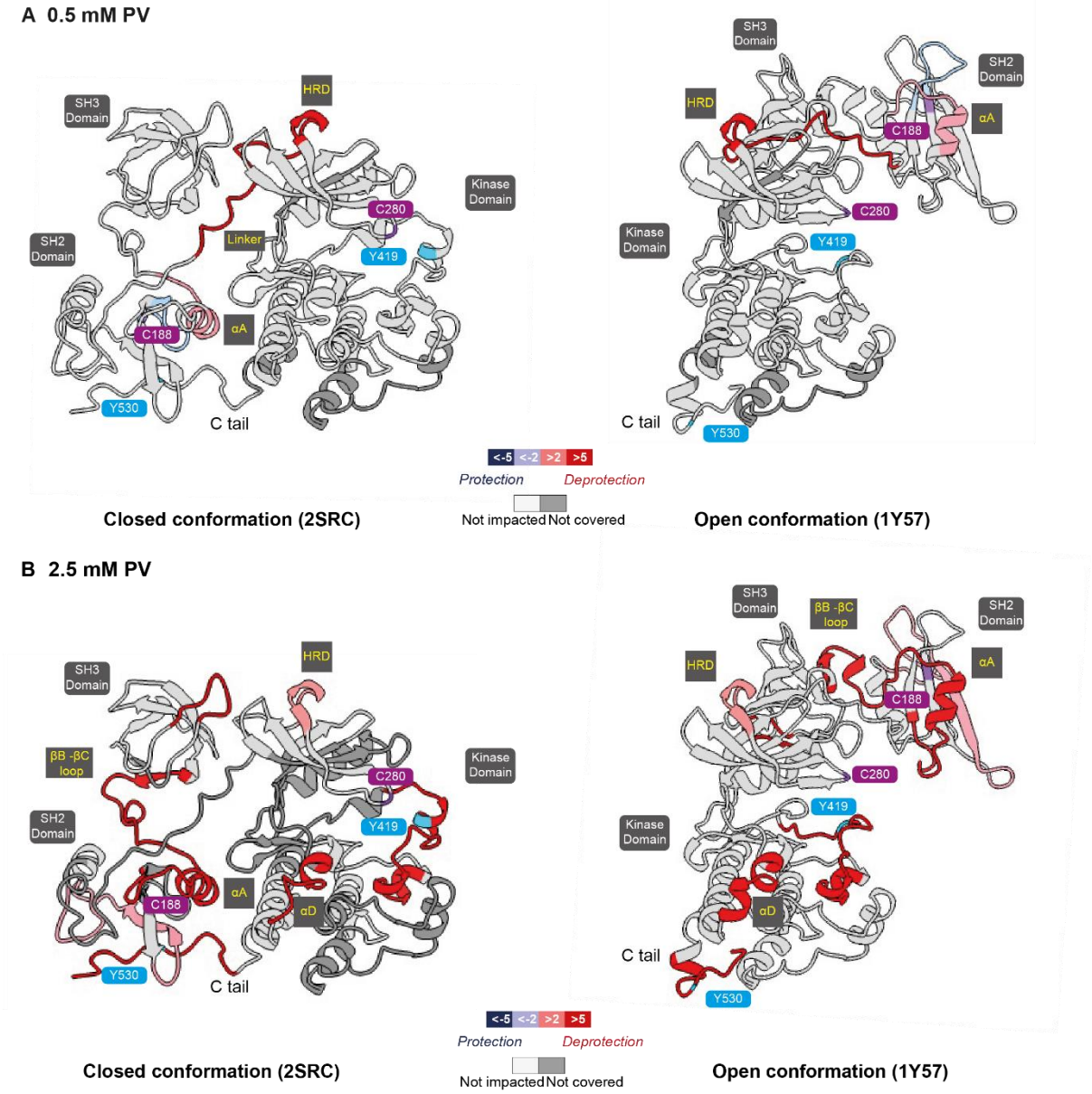

Fig. 3. PV induces specific conformational changes in SRC.
(A, B) HDX-MS analysis of pervanadate treated SRC. Relative fractional uptake (RFU) differences between 5 μM SRC and SRC incubated with 0.5 mM (**A**) and 2.5 mM (**B**) PV were mapped on the closed (Left) and the open conformations (Right) of SRC (PDB: 2SRC and 1Y57, respectively). Regions showing significant protection and becoming less solvent exposed are colored in blue and regions showing significant deprotection and becoming more solvent exposed are presented in red. Regions where no significant differences were observed are shown in white, while grey denotes parts of SRC for which no peptides were observed. Key cysteines are highlighted in purple and key phosphorylation sites are highlighted in light blue. The overall coverages were 80% and 60% for the 0.5 mM and 2.5 mM PV HDX-MS experiments, respectively.

See also Fig. S4.

301
302 **PV triggers conformational changes that relieve SRC autoinhibition**
303 We next performed a mechanistic investigation into SRC activation by oxidation. Previous
304 molecular dynamics simulation suggested that cysteine oxidation plays a role in relieving
305 autoinhibition (*21*), a key step in SRC activation. SRC autoinhibition is mediated by
306 intramolecular contacts between SH2 and SH3 domains and the kinase domain (*35, 36*), with
307 extensive conformational changes occurring during activation. To evaluate whether oxidation
308 promotes conformational changes in SRC, we initially used a thermal shift assay using affinity
309 purified proteins. ATP and Dasatinib stabilized full-length recombinant SRC, whereas PV and
310 H_2O_2 led to destabilization, indicating oxidation-induced conformational changes (**Fig. S4A**).
311
312 To obtain a detailed molecular understanding of conformational changes caused by PV, we
313 used hydrogen-deuterium exchange MS (HDX-MS) on full-length human SRC. The relative
314 deuterium uptake differences were mapped onto the 'closed' (2SRC (*37*)) and 'open' (1Y57
315 (*38*)) SRC conformations (**Figs. 3A-3B**). At 0.5 mM (100x molar ratio of PV to SRC), PV
316 increased solvent exposure of the SH2-kinase domain linker, which spans the polyproline-II
317 helix. This helix engages the SH3 domain in the autoinhibited conformation and is released
318 upon activation (**Figs. 3A *right,* and S4B**) (*35, 36*). In the SH2 domain, PV induced exposure
319 of the αA helix while protecting the βB-βC loop, indicating redox-sensitive conformational
320 changes near Cys 188. This suggests that 0.5 mM PV drives two key structural alterations
321 involved in SRC activation.
322
323 At 2.5 mM (500x molar ratio of PV to SRC), PV induced extensive solvent exposure across
324 SRC regions associated with conformational transition from inactive to active kinase (**Fig. 3B**).
325 The RT loop and the βE strand within the SH3 domain showed increased exchange, indicating
326 release from the polyproline-II linker (*39*), a more pronounced effect than with 0.5 mM PV (**Fig.**
327 **3A**). Changes in the SH2 domain were also more prominent at this higher PV concentration
328 (**Figs. 3B and S4C**). In the linker between the SH3 and kinase domains, a region spanning
329 Trp 263 was exposed by PV. This key conserved residue is involved in forming a new β turn
330 during the transition from closed to open conformations (*40*). The activation loop, including Tyr
331 419, was also more exposed aligning with previous MD simulations predicting Cys 280
332 oxidation-induced unfolding of this loop (*21*). The catalytic loop HRD motif and the αEF helix,
333 which stabilize the activation segment in an active state, were also more exposed upon PV
334 treatment (*37, 38, 41*) (**Fig. 3B, *right***). The C-terminal tail, including Tyr 530, was more
335 accessible along with the αD helix (**Fig. 3B, *right***). Overall, PV induced conformational
336 changes that increased flexibility and solvent accessibility, explaining the oxidation-induced
337 destabilization observed by thermal shift (**Fig. S4A**). These effects were increased at 2.5 mM
338 PV, consistent with the dose-dependent effects observed in kinase assays (**Fig. 2A**).
339 Together, these results support a model in which PV drives the relief of SRC autoinhibition via
340 specific conformational alterations across the polypeptide. Furthermore, at lower levels of
341 oxidation we observed conformational changes largely in the vicinity of Cys 188, aligning with
342 its greater sensitivity to oxidation (**Figs. 2E and 2F**), with effects mediated by Cys 280
343 requiring increased PV levels. This supports a hierarchy of cysteine PV sensitivity within SRC.
344

Figure 4

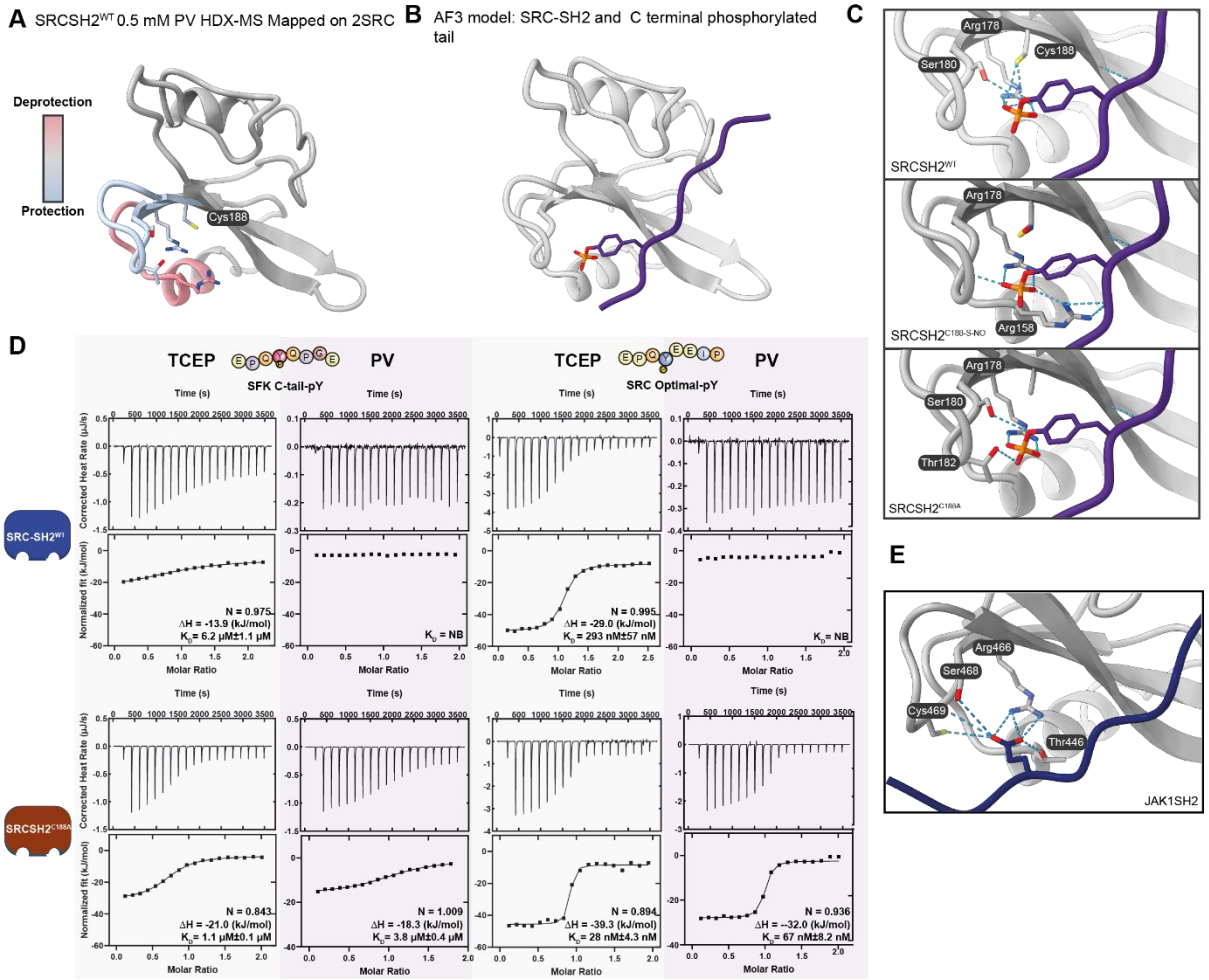

Fig. 4. **Cys 188 oxidation or mutation impacts SRC-SH2 phosphopeptide binding.** (**A**) SRC-SH2 with highlighted regions protected (blue) and deprotected (red) from deuterium exchange upon 0.5 mM PV treatment (PDB:2SRC) based on data from Fig. 3. (**B**) Alphafold3 (*42*) model of SRC SH2^{WT} bound to the phosphorylated SRC C-terminal peptide: FTSTEPQpYQPGENL. ipTM = 0.73. (**C**) Residues predicted to form hydrogen bonds (blue dashed lines) based on AF3 models. Top: As in B. Middle: AF3 model with SRC s-nitroso cysteine 188 and C terminal peptide. ipTM = 0.75. Bottom: AF3 model with C188A and C terminal peptide. ipTM = 0.72. (**D**) Isothermal titration calorimetry (ITC) titration curves of the interaction between SRC-SH2 and indicated phosphopeptides. The SH2 domain was pretreated with 1 mM TCEP or 0.1 mM PV prior to the assay. Upper: baseline-corrected differential power plotted over time. Lower: normalized binding curve showing the integrated change in enthalpy against the molar ratio. Stoichiometry (N), mean enthalpy change (ΔH) and mean K_D ±SD shown based on n =3 assays. (**E**) AF3 model of hydrogen bonding network between residues within the JAK1 SH2 domain engaging glutamate on IFNR1. ipTM = 0.69.

See also Fig. S5.

364 **Cys 188 oxidation impacts SRC-SH2 affinity for phosphopeptides**
365 We next focused on how the conformational changes within the SRC SH2 domain revealed
366 by our HDX-MS data may contribute to relief of autoinhibition (**Fig. 4A**). Cys 188 resides within
367 the pTyr binding pocket and is ideally placed to mediate SRC interactions with
368 phosphopeptides (**Figs. 4A-4B**). We used AlphaFold3 to explore the binding of SRC-SH2
369 domain with the phosphorylated SRC C-terminal peptide, which interact in the autoinhibited
370 state (*42*). Cys 188 is predicted to participate in a hydrogen bonding network that engages the
371 phosphate group of the bound peptide (**Figs. 4C, *Top* and S5A**). To mimic the effects of
372 oxidation, we modelled Cys 188 with an S-nitroso modification in AlphaFold3 (**Figs. 4C,**
373 ***middle* and S5B**). We infer that Cys oxidation causes extensive remodelling of the hydrogen-
374 bonding network, reducing the overall number of contacts with the phosphate group. In
375 contrast, modelling C188A predicts hydrogen bonding network adjustments that incorporate
376 new interactions, including with Thr 182 (**Figs. 4C, *bottom* and S5C**), which might impact
377 phosphopeptide binding.
378
379 We next used isothermal titration calorimetry (ITC) to quantify effects of PV on phosphopeptide
380 interaction dynamics using WT and C188A SRC-SH2 domains (**Fig. 4D**). As predicted by our
381 AlphaFold3 analysis (**Fig. 4C, *bottom***), under reducing conditions (1 mM TCEP), SRC-
382 $SH2^{C188A}$ showed a 5-fold increase in affinity for the SRC C-terminal phosphopeptide
383 (spanning pY530) compared to $SH2^{WT}$ (**Fig. 4D**). Strikingly, oxidation of $SH2^{WT}$ with 0.1 mM
384 PV abolished phosphopeptide binding, consistent with uncoupling of the inhibitory complex.
385 In marked contrast, there was still detectable binding to $SH2^{C188A}$, albeit with ~3.5-fold lower
386 affinity than under reducing conditions. Next, we examined interactions with an optimised SRC
387 binding phosphopeptide (EPQ**pY**EEIP) (*43*). We detected a ~10-fold increase in affinity with
388 $SH2^{C188A}$ compared to $SH2^{WT}$, consistent with a previous study (*44*) (**Fig. 4D, *lower***).
389 Strikingly, PV treatment eliminated phosphopeptide binding by $SH2^{WT}$, but not $SH2^{C188A}$, which
390 showed a ~3-fold decrease in affinity compared to TCEP-treated samples (**Fig. 4D**). Both Cys
391 241 and Cys 248 are present within the SH2 domain and may contribute to this residual PV
392 sensing. Nevertheless, our results support Cys 188 in mediating SRC-SH2 phosphopeptide
393 binding and sensitivity to PV. These findings provide a plausible mechanistic explanation for
394 the impact of Cys 188 oxidation on the activity of SRC in cells.
395
396 Finally, we asked whether other human SH2 domains possess putative redox sensitive
397 cysteines that could alter phosphopeptide interactions. Interestingly, SH2D1A, SH2D1B and
398 SH2D5 all possess a cysteine analogous to SRC Cys 188 (**Fig. S5D**). Furthermore, a mutation
399 affecting this cysteine in the SH2D1A domain is linked to lymphoproliferative disease (*45*).
400 Several signaling proteins also possess SH2 domains with cysteine residues within their pTyr
401 binding pockets (*46*) (**Fig. S5E**), including the PTKs Zap70 and Syk, which exhibit reduced
402 phosphopeptide binding following oxidation by H_2O_2 (*47*). We anticipate that cysteine residues
403 (*46*) within the CLNK and JAK1-SH2 domains would also regulate signaling in a redox-
404 sensitive manner (**Figs. 4E and S5E**). Thus, redox-regulated SH2 domain-phosphopeptide
405 interactions are important beyond SRC.
406
407 **Mutational relief of SRC autoinhibition bypasses the functions of Cys 188 and Cys 280**
408 **in cells**
409 Mutating SRC Tyr 530 (Y530F) favours its open, active conformation (*48*). We hypothesized
410 that this mutation would render SRC less sensitive to the effects of cysteine mutation and
411 activation by oxidation. To test this, we introduced SRC^{Y530F} and dual mutant variants

412 $SRC^{Y530F;C188A}$ and $SRC^{Y530F;C280A}$ into SYF KO MEFs. As expected, basal pY419 and global
413 pTyr signal in cells expressing SRC^{Y530F} was increased compared to those expressing SRC^{WT}
414 (**Figs. 5A and S6A**). SRC^{C188A} and SRC^{C280A} showed a striking increase in pY530 and
415 reciprocally diminished pY419, indicating increased autoinhibition. In contrast, introducing the
416 Y530F mutation overcame the inhibitory effects of C188A and C280A in unstimulated cells,
417 as determined by pY419 levels (**Figs. 5A and S6A**). PV stimulated global pTyr equivalently
418 for all SRC^{Y530F} variants independently of Cys 188 or Cys 280 mutations. In contrast, PV-
419 induced pTyr levels were lower for SRC^{WT} cysteine mutations. We also noted that SRC pY530,
420 a reported substrate of numerous PTPs (*49-51*), was unchanged by PV treatment (**Fig. 5A**).
421 These results support that Cys 188 and Cys 280 regulate SRC activity at the level of
422 autoinhibition in cells. Aligning with this, SRC Cys 188 and Cys 280 have been implicated in
423 transducing signals downstream of ATP (*21*) and IL33 (*52*) stimulations.
424
425 **SRC Cys 188 and Cys 280 are required for overcoming cell contact inhibition**
426 Reintroducing SRC^{WT} into SYF KO MEFs stimulated proliferation (**Fig. 5B**). This effect was
427 not recapitulated by expression of SRC^{C188A} or SRC^{C280A}, reflecting the reduced basal cellular
428 activity of these mutants (**Fig. 5B**). In contrast, constitutively active SRC^{Y530F} increased cell
429 growth regardless of C188A and C280A mutations. Notably, $SRC^{Y530F;\ C188A}$ cells exhibited the
430 highest growth rate (**Fig. 5B**), potentially reflecting a negative impact of Cys 188 oxidation,
431 which would impair pY530 binding but would subsequently also limit binding to and recruitment
432 of other phosphoproteins (**Fig. 4**). We observed that differences in cell number were largely
433 driven by post-confluent growth. Indeed, SRC^{WT} and SRC^{Y530F} expressing cells did not
434 undergo contact inhibition, whereas SYF KO, SRC^{C188A} and SRC^{C280A} cell lines did (**Fig. 5B**
435 **and movies S3-S6**). Following growth to post-confluence, SRC^{WT} expressing cultures had
436 significantly more nuclei supporting increased cell proliferation compared to either the SYF
437 KO or SRC^{C188A} and SRC^{C280A} (**Figs. 5C-5D**). Together, these findings demonstrate that SRC
438 Cys 188 and Cys 280 are required to drive cell overgrowth.
439
440 The Hippo pathway is a conserved regulator of contact inhibition of cell growth (*53*). We next
441 tested whether SRC-dependent cellular overgrowth phenotypes were associated with YAP
442 activation (*53*). Compared to WT, SYF KO MEFs displayed increased YAP phosphorylation at
443 Ser 127 (**Fig. 5E**), a site associated with its cytoplasmic sequestration and inactivation. This
444 trend was recapitulated by phosphorylation of the upstream Hippo pathway kinase LATS1
445 (**Figs. 5E and S6B**). Consistently, expression of SRC^{WT} was sufficient to suppress YAP
446 phosphorylation, whereas SRC^{C188A} and SRC^{C280A} resembled SYF KO cells, with elevated
447 levels of YAP phosphorylation, despite comparable SRC expression levels (**Fig. 5E**). In
448 conclusion, SRC redox-sensitive cysteines are required for YAP activation, correlating with
449 the ability of cells to overcome contact inhibition of proliferation.
450

Figure 5

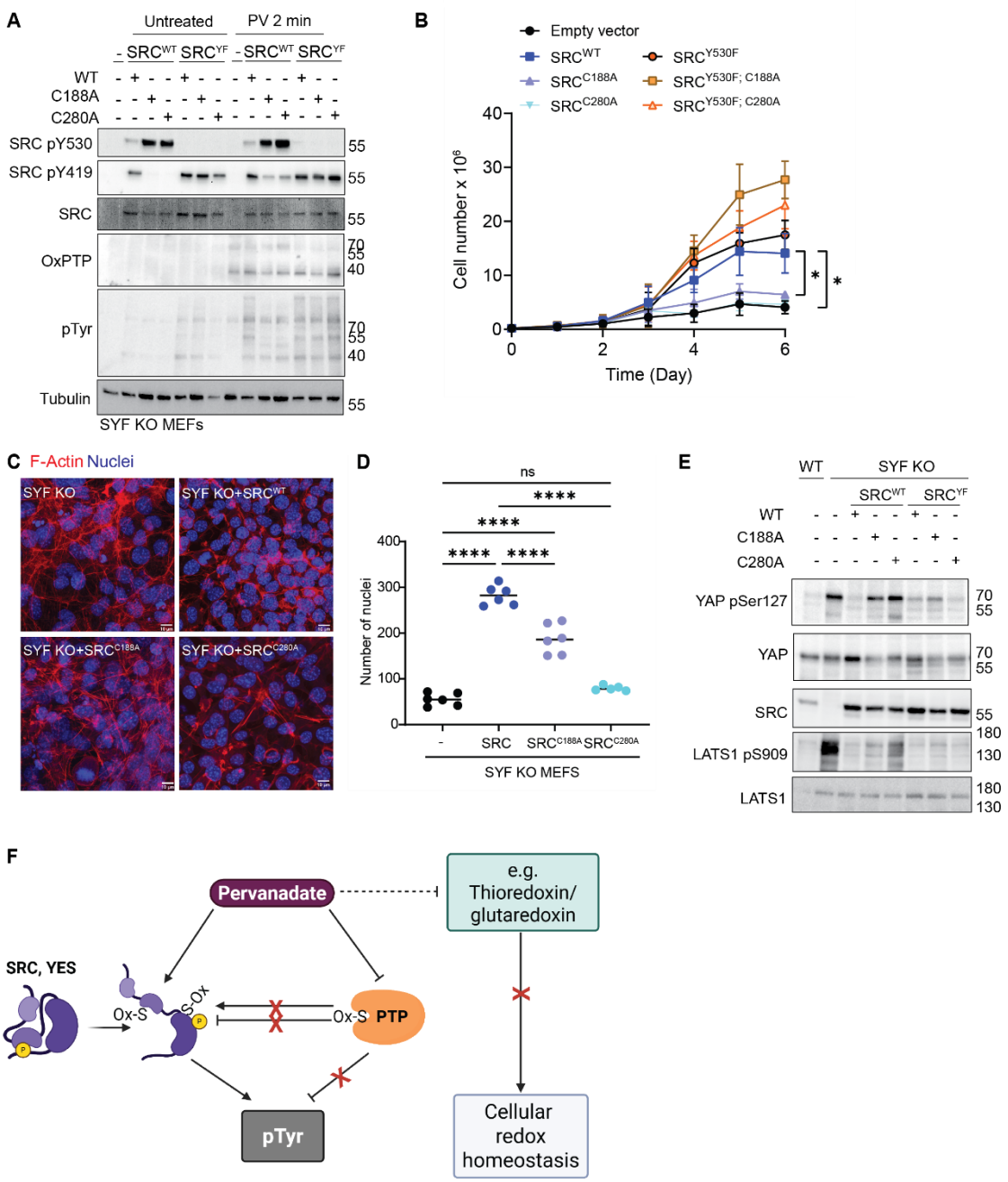

Fig. 5. SRC cysteines are required to overcome contact inhibition

(**A**) SYF KO MEFs were retrovirally transduced with specified SRC expression constructs and treated with 100 μM PV as shown, before lysis and immunoblotting with indicated antibodies. (**B**) Cell numbers were determined over time in culture for SYF KO MEFs, retrovirally transduced with specified SRC expression constructs (as in A). (**C**) Confocal microscopy images of SYF KO MEFs complemented with the indicated constructs grown to post-confluence, fixed, permeabilized and stained with the DAPI (nuclei; blue) and Phalloidin (actin; red). (**D**) Quantification of nuclei taken from 5 or 6 fields of view per cell line. **** p.Adj < 0.001. Ordinary one-way ANOVA with Tukey's correction for multiple comparisons. (**E**) SYF KO MEFs expressing the indicated constructs were grown to post-confluence, lysed and immunoblotted with the indicated antibodies. Representative blot from n=3 experiments. (**F**) In summary, Pervanadate induces numerous cellular changes. Increases in pTyr can be

464 attributed to the hyperoxidation of PTP catalytic cysteines as well as direct oxidation of specific
465 cysteines on SRC and YES leading to relief of autoinhibition and activation. Furthermore, PV
466 induces rapid oxidation of HyPer7, a reporter for both H2O2 and the activity of cellular
467 antioxidant systems such as thioredoxin and glutaredoxin. PV therefore disrupts redox
468 homeostasis in addition to increasing phosphotyrosine levels.
469
470 See also Fig. S6
471

472 **Discussion**
473
474 PV is a commonly used PTP inhibitor that has shaped our understanding of pTyr-based
475 regulation and the study of PTP-substrate interactions (*54, 55*). Our work demonstrates that
476 PV can disrupt cellular redox homeostasis, leading to oxidation of HyPer7 and PRDX1, but
477 also shows selectivity, directly targeting cysteines within positively charged protein surfaces.
478 Using a series of mutational approaches, enzyme assays and cellular studies, we find that the
479 potent effects of PV on global pTyr are best explained by the combined inhibition of PTPs and
480 the direct oxidation and activation of SFKs, and perhaps other PTKs, such as Eph receptors
481 (*56*). This finding should prompt a re-evaluation of the use and interpretation of experimental
482 data generated using PV treatments.
483
484 Based on the oxidation of both HyPer7 and PRDX1, PV must interfere with antioxidant
485 pathways, particularly the redoxins that can directly or indirectly reduce both proteins. One
486 possibility is that it reacts with and depletes reduced glutathione (GSH) or NADPH. PV
487 probably evades H_2O_2-reactive PRDX, enabling it to target additional cysteine thiols similarly
488 to what has been observed for *cis*Trp-OOH (*57*). This would be consistent with rapid PTP
489 hyperoxidation. Over time, PV induces PRDX1 tyrosine phosphorylation, potentially enabling
490 endogenous H_2O_2 to oxidise cysteine thiols (*32*). Interestingly, the SRC cysteine residues
491 studied here showed a distinct pattern of sensitivity to H_2O_2 than we observe for PV (*21*).
492 Therefore, we propose that PV preferentially targets PTP active sites, as well as other
493 phosphate-binding pockets, including the SRC kinase active site (Cys 280) and SH2 domain
494 (Cys 188), correlating with protein regions with high positive charge (**Fig. 2G**). In contrast,
495 mercuric chloride activates SRC independently of autoinhibition via Cys 486 and 501, which
496 are surrounded by negative charge, particularly in the open conformation (*58*). Therefore, SRC
497 responds differentially to distinct oxidants.
498
499 Cys 188 is located at an equivalent position to Thr 42 in the N-terminal SHP2 SH2 domain,
500 which is mutated in disease and alters phosphopeptide specificity (*59*). Likewise, SRC-
501 $SH2^{C188A}$ altered affinity for phosphopeptides, but also impacted redox sensitivity.
502 Interestingly, Cys 188 reportedly forms a disulfide bridge with a cysteine residue of its
503 substrate cortactin (*60*), which could explain the greater influence of mutating this cysteine in
504 cells than *in vitro*. Cys 188 oxidation is likely to play two roles: firstly, decreasing affinity for
505 phosphopeptides and promoting relief of autoinhibition. and secondly, mediating disulfide
506 bridge formation with interaction partners, an intriguing area for further investigation. Amongst
507 SFK cysteine residues, Cys 188 exhibits the highest level of reversible oxidation in mouse
508 tissues, supporting the physiological relevance of our findings (*20, 61*). We further identified
509 other SH2 domain pTyr pocket cysteine residues. Zap70 possesses a redox-sensitive pTyr
510 binding pocket in its N terminal SH2 domain, but has a distinct mode of autoinhibition
511 compared to SRC (*62*). Thus, oxidation of this cysteine may negatively impact ZAP70
512 recruitment to phosphorylated immunoreceptor tyrosine-based activation motifs (ITAMs) (*47*)
513 but may also mediate intermolecular disulfide interactions. Interestingly, CSK, which promotes
514 SRC Tyr 530 phosphorylation and subsequent inhibition, is regulated *in vitro* via an
515 intramolecular disulfide bond involving its SH2 domain and could also contribute to redox and
516 pTyr signalling integration (*63*). Thus, redox regulation of SH2 domains is a wider area for
517 future investigation.
518

519 SRC^{C188A} and SRC^{C280A} expressing cells showed a striking increase in pY530, which differs
520 from previous reports (*21*). One explanation for this difference is that we 'rescued' SRC-
521 deficient cells, whereas other studies were performed in the presence of endogenous SRC
522 (*21*). Furthermore, we have employed untagged SRC wherever possible, since both the N and
523 C termini of SRC contain important regulatory elements. For example, a C terminal affinity tag
524 could interfere with autoinhibition, whilst N-terminal tags would block N-myristoylation, which
525 is important for localisation (*64*). This striking increase in pY530 (**Fig. 5A**) may be consistent
526 with the preservation of an autoinhibited state and protection from dephosphorylation by a
527 stabilized SH2 domain interaction. Alternatively, it could represent an increase in CSK activity,
528 although this has not been mechanistically explored in this study.
529
530 In *Drosophila*, Src42A Cys 471, equivalent to human SRC Cys 490, is implicated in wound
531 healing responses (*65*), and may form an intramolecular disulphide with Cys 248 (*19*). Neither
532 Cys 188 nor Cys 280 are conserved in *Drosophila* Src (42A or 64B), but are conserved in
533 zebrafish and chicken, indicating multiple layers of SRC redox regulation acquired during
534 evolution. SRC can be S-glutathionylated at Cys 400 leading to inhibition of
535 autophosphorylation, linking its cellular regulation to this pathway (*66*). How SRC cysteines
536 undergo oxidation and reduction *in vivo* remains an important question, particularly given the
537 relatively high oxidant concentrations required to elicit changes in activity *in vitro*.
538
539 SRC is a proto-oncogene yet rarely mutated in human cancers (*67*). Cys 188 and Cys 280
540 mutations prevent SRC mediated cell overgrowth, strongly suggesting that the oxidative
541 environment typical of some cancers (*68*) could drive relief of SRC autoinhibition,
542 phenocopying Y530F or C-terminal truncations (*67*). Our findings with the conserved Cys 280
543 residue also have implications for YES1, for which we also demonstrate oxidative activation
544 by PV (**Fig. S3G**). Interestingly, the equivalent cysteine in YES1 (Cys 287) has previously
545 been targeted with a covalent inhibitor (*69*). Our finding that non-catalytic redox-sensing Cys
546 residues in PTKs is a dominant signaling mechanism potentially increases their attractiveness
547 as therapeutic targets, especially if greater potential for selectivity than active site inhibitors
548 can be achieved (*70*).
549
550 **Materials and methods**
551 **Plasmids and constructs**
552 Amino acid (aa) numbering is based on the following sequences: Human PTPRK; UniProt ID:
553 Q15262-3, Human SRC; Uniprot ID: P12931-1, Chicken Src Uniprot ID: P00523. Generation
554 of bacterially expressed (aa 864–1446) and mammalian overexpression PTPRK intracellular
555 domain (aa 776-1446) constructs were previously described (*73, 74*). Full length human SRC
556 containing a 3C-protease cleavable, N-terminal, tandem Strep-tag II was cloned into pcDNA3.
557 Human rhinovirus 14 3C protease plasmid (pET-NT*-HRV3CP) was a gift from Gottfried Otting
558 (Addgene # 162795).
559
560 The retroviral pLNCX chicken Src Y527F plasmid was a gift from Joan Brugge (Addgene
561 #13660). HyPer7 (*30*) (a gift from Vsevolod Belousov (Addgene #136464)) was fused in-frame
562 downstream of the SRC myristylation sequence to make the 'PM-HyPer7' biosensor and
563 subcloned into pLJM1 (gift from Joshua Mendell (Addgene #91980)). N-terminally His-tagged
564 HyPer7 was cloned into the pQE30 vector. The cDNA encoding the human SRC SH2 domain
565 (Gln147-Lys252) was subcloned into the pETM11 vector (a gift from Elisa Izaurralde (Addgene

566 #145950)). The QuikChange II mutagenesis kit (Agilent) was used to construct the mutant
567 SRC SH2 domains.
568
569 All other point mutations were introduced by polymerase chain reaction (PCR) using either Q5
570 High-Fidelity DNA (New England Biolabs, UK), CloneAmp (Takara) or Phusion Hot Start II
571 DNA (Thermo Fisher Scientific) polymerases as per manufacturer's protocol.
572
573 **Cell culture and treatments**
574 HEK293T, U2OS and SYF KO MEFs (CRL-2469) cells were purchased from ATCC. WT MEFs
575 were generated in-house, described below. SRC WT and KO HAP1 cells were purchased
576 from Horizon (HZGHC000348c023). Plat-E cells were donated by P. Hawkins and L. Stephens
577 (Babraham Institute) and were purchased from Cell Biolabs Inc (RV-101). Cells were
578 maintained in 75 cm^2 vented tissue culture flasks in a 37°C humidified 5% CO_2 ventilator and
579 passaged using trypsin-EDTA solution (Sigma-Aldrich), prior to reaching confluence every 2-
580 4 days. HEK293T and MEF cells were grown in DMEM containing 10% (v/v) fetal bovine serum
581 (FBS; Sigma-Aldrich), 2 mM L-glutamine (Sigma-Aldrich). U2OS cells were grown in McCoy's
582 5A medium modified with 10 % (v/v) FBS (Sigma-Aldrich). HAP1 cells were cultured in IMDM
583 containing 10% (v/v) fetal bovine serum (FBS; Sigma-Aldrich, with Plat-E cells cultured in
584 DMEM (high glucose with L-glutamine and pyruvate supplemented) containing 10 % heat-
585 inactivated FBS (Sigma-Aldrich) with additional blasticidin (10 mg/ml) and puromycin (1
586 mg/ml) when in culture for more than 2 passages. All cell lines are routinely mycoplasma
587 tested using MycoProbe Mycoplasma Detection Kit (R&D system) or MycoAlertTM (Lonza
588 Bioscience).
589
590 **MEF line generation**
591 WT (Bl6/N) MEFs were generated in-house. Following dissection, E13-14 embryos were
592 placed into PBS on ice. Placental and maternal tissues and head were removed prior to
593 tryspinization and dissociation with a razor blade. DNAseI was then added followed by
594 incubation at 37°C for 10 min. DMEM with 10 % FBS was added to quench trypsin. Cells were
595 pipetted through a 40 µm filter and pelleted at 140 x g for 5 min. Finally, cells were
596 resuspended in DMEM with 10% FBS, 2 mM L-glutamine and pen-strep then seeded for
597 culturing. Cells were cryopreserved in liquid N2 in 50% FBS:10% DMSO:40% DMEM for future
598 use.
599
600 **Small molecules and growth factors**
601 The following inhibitors were purchased from Sigma: Dasatinib (SML2589-50MG), focal
602 adhesion kinase inhibitor 1 (324877-5MG), Gefitinib (SML1657-10MG), Ibrutinib (PZ0242-
603 5MG), Imatinib (CDS022173-25MG), Lapatinib (SML2259-10MG), Nilotinib (SML3799-
604 10MG), PP2 inhibitor (529573-1MG), Saracatinib (SML3195-5MG) and SU6656 (S9692-5mg).
605 Inhibitors were re-suspended in DMSO. The following growth factors were purchased from
606 Qkine: PDGF (Qk044), IGF1 (Qk047), FGF2 (Qk025), TGFβ2 (Qk072). Insulin was purchased
607 from Scientific Laboratory supplies (I5500) and EGF was purchased from Peprotech (AF-100-
608 15).
609 **Antibodies and dyes**
610 Antibodies against the following target proteins or epitopes were used in the study:
611 Phosphotyrosine (Cell Signaling Technology (CST) #8954S), α Tubulin (Sigma #T6199), Flag
612 (CST #8146S), Pan-SFK (CST #2108), SRC family pY416 (#CST D49G4), SRC pY530 (CST
613 #2105), SRC-specific (CST #2123 & #2120), oxPTP (R&D Systems # MAB2844), His (CST

#12698S), ABL1 (c-Abl) (CST #2862), ABL1 (c-Abl) pY412 (CST #2865S), Cortactin (CST #3503), Cortactin pY421 (CST #4569), LATS1 (CST #3477), LATS1 pY909 (CST#9157) , YAP (CST #4912), YAP pS127 (CST #13008), AKT (CST #9272), AKT pS473 (CST #4060), ERK pT202/pY204 (CST #4370), ERK (CST #4696), EGFR (CST #2232S), EGFR pY1068 (CST #3777S), SHP2 (CST #3397), PRDX1 pY194 (CST #14041), PRDX1 (CST #8499). HRP-conjugated secondary antibodies were purchased from Jackson Immunoresearch(#715-035-150 & #711-035-152). Hoechst and BODIPY Phalloidin 558/568 (B3475) was purchased from Thermo Fisher Scientific.

Pervanadate stock generation

Pervanadate was generated as previously described (*6*). To avoid decomposition, it was prepared immediately prior to use. In a 1.5 ml tube, 100 µl of activated pH 10 100 mM sodium orthovanadate (Alfa Aesar 15403009) was combined with 103 µl 0.49 M H_2O_2 in 20 mM HEPES, pH 7.3, mixed by gentle inversion and incubated at RT for 5 min. Excess H_2O_2 was quenched by addition of 23 µl of 0.5 mg/ml catalase in 50 mM potassium phosphate, followed by mixing by gentle inversion, yielding a 44.2 mM pervanadate stock solution for immediate use.

Recombinant proteins and synthesized peptides

Peptides were obtained at 95% purity from Biosynth. The SRC peptide substrate 5-FAM-EGIYGVLFKKK-CONH2 was synthesized by Genscript. Recombinant N-terminal His6-tagged SRC (1-536) kinase fusion protein (DU19041) and N-terminal His6-tagged YES1 (1-543) (DU5884) was purified from Sf21 cells was purchased from Medical Research Council Protein Phosphorylation and Ubiquitylation Unit (PPUU) reagents and services (University of Dundee). N-terminally His-tagged Hyper7 (*30*), PTPRK ICD (*73*), SRC SH2 domain and His6-tagged 3C protease (*75*) were purified using standard affinity and size exclusion chromatography methods and stored −80°C as follows*:*

M15 Escherichia coli cells were transformed with N-terminally His-tagged Hyper7 construct and cultured in LB Broth at 37°C to OD600nm ~0.5-0.8 and induced with 400 µM isopropyl-thio-β-D-galactopyranoside (IPTG Thermo Fisher Scientific, dioxane-free) for 14 h at 16°C. *Escherichia coli* BL21(DE3) Rosetta cells transformed with SRC SH2 construct or the other aforementioned constructs were cultured at 30~~7~~°C/220 rpm in LB broth containing 34 µg/ml chloramphenicol until the OD600 nm reached 0.5–0.8 or cultured at 30°C/220 rpm in 1 L 2XTY medium containing 50 µg/ml carbenicillin and 34 µg/ml chloramphenicol until the OD600 reached 0.6–0.7 respectively. Cultures for SRC SH2 were transferred to 16°C/220 rpm and induced with 100 µM IPTG (Thermo Fisher Scientific, dioxane-free) for 14 h. All other constructs were transferred to 20°C/220 rpm and allowed to equilibrate, prior to the addition of 1 mM IPTG (Generon) for 20h. PTPRK cultures were also supplemented with 200 µM of D-biotin (Sigma-Aldrich) upon IPTG addition. Cells were harvested by centrifugation at 4000 x g for 20-30 mins and bacterial pellets were stored at – 20°C until required.

For Hyper7, pellets were resuspended in lysis buffer (40 mM HEPES, pH 7.4, 400 mM NaCl, 10% (v/v) glycerol, 1 mM benzamidine, 1 mg/mL Leupeptin, 0.1 mg/mL 4-(2-aminoethyl) benzenesulfonyl fluoride hydrochloride (AESBF), 100 mg/mL DNaseI, 20 mM MgCl2) or oxidizing or reducing lysis buffer for SRC SH2 domains (20 mM HEPES (pH 7.5), 100 mM NaCl, and 0.1 mM pervanadate; reducing SH2 buffer: 20 mM HEPES (pH 7.5), 100 mM NaCl, and 1 mM TCEP). Once re-suspended in lysis buffer, samples were lysed by sonication and

clarified by centrifugation at 39,000 x g for 30 min at 4°C. For PTPRK and 3C protease proteins, cells were lysed in purification buffer (50 mM HEPES pH 7.5, 500 mM NaCl, 5% (v/v) glycerol and 0.5 mM tris (2-carboxyethyl)phosphine (TCEP)), containing EDTA-free protease inhibitor tablets (Roche) followed by cell disruption using a Constant Systems cell disruptor and then lysate clarification via centrifugation at 40000 x g for 30 min at 4°C. His-HyPer7 were purified by affinity chromatography (Ni2+- Sepharose (GE Healthcare) and imidazole-based elution) and size exclusion chromatography using a HiLoad 16/600 Superdex 200 column (GE Healthcare) equilibrated in 50 mM Tris-HCl (pH 7.4), 100 mM NaCl, and 10% (v/v) glycerol. SH2 domains were purified with pre-equilibrated nickel column (His-Trap HP, GE Healthcare) and the 6x His-tag was removed by digestion with home-made tobacco etch virus protease at 4°C for 12 h accompanied with oxidizing buffer and reducing buffer.

SH2 domains were further purified on a Superdex 75 10/300 GL size exclusion column (GE Healthcare) with oxidizing buffer and reducing buffer. For PTPRK and 3C protease, the supernatant was removed and incubated with 0.5 ml of Ni-NTA agarose (Qiagen) for 1 h at 4°C. Ni-NTA Agarose was then pelleted via centrifugation at 500 x g for 5 min at 4°C and packed into a gravity flow column. Ni-NTA agarose was then washed with 10 volumes of purification buffer containing 5 mM imidazole, followed by 20 volumes of purification buffer containing 20 mM imidazole; prior to elution in purification buffer containing 250 mM imidazole. The eluted protein was then subjected to size exclusion chromatography (SEC) using a Superdex 200 16/600 column (GE Healthcare Life Sciences, Thermo Fisher Scientific). Columns were equilibrated in SEC buffer (50 mM HEPES pH 7.5 (50 mM Tris pH 7.4 for SH2 domains), 150 mM NaCl, 5% (v/v) glycerol, 5 mM DTT). Protein was concentrated to 2–10 mg/ml using an Ultracel-10K regenerated cellulose centrifugal filter (Merck Millipore). Proteins were either used fresh or snap-frozen for storage at -80°C until required.

Generation of stable cell lines

SRC-rescued SYF KO MEF cell lines were generated using the retroviral expression system. Retrovirus was generated through the reverse transfection of Plat-E cells (12 x 10^6) in 15 cm^2 dishes with 16.8 µg pLNCX construct DNA into 2 ml OPTIMEM (Gibco) with 50.4 µl Lipofectamine 2000 transfection reagent (Invitrogen) following the manufacturer's instructions. Media was replaced with 9 ml complete MEF media per 15 cm^2 dish 20-24 hours post-transfection. 48-72 h post-transfection, retrovirus was harvested from Plat-E cell media by centrifugation for 5 min at 800 x g (RT) and filtered through a 0.2 µm syringe filter (Sartorius) before either freezing at -80°C or adding directly onto MEF SYF KO cells after dilution 1:1 into MEF culture media, in 6-well dishes. Media was replaced 24 h after adding viral supernatant, followed by at least two passages before experimental analysis.

For lentiviral generation, 1.5×10^7 HEK293T cells were seeded in 12 ml of complete growth medium per 15 cm^2 dish (two dishes per lentivirus) and incubated for 24 h at 37°C with 5% CO_2. Each 15 cm^2 dish was then transfected with 6 µg of pLJM.PM-HyPer7, 12 µg psPAX2 packing plasmid (Addgene #12260, deposited by Didier Trono) and 3 µg pMD2.G envelope plasmid (Addgene #12259, deposited by Didier Trono) using the GeneJuice transfection reagent (Merck Millipore, UK) as per manufacturer's instructions. After 24 h, the medium was then replaced with 16 ml complete growth medium. At 48–72 h post-transfection, culture medium was collected and filtered through a 0.2 µm syringe filter (Sartorius). Viral particles were concentrated using Lenti-X concentrator as per manufacturer's instructions (Takara Bio). Lentivirus was centrifuged at 1500 x g for 45 min at 4°C, resuspended with complete DMEM

710 media and aliquoted and stored at −80°C until required. 2×10^5 U2OS cells were seeded per
711 well of a six-well plate in 900 µl of growth medium, prior to the drop-wise addition of 100 µl
712 concentrated lentivirus. After 30 min at room temperature, the cells were returned to the
713 incubator. 72 h later, cells were reseeded in 1 µg/ml puromycin (Thermo Fisher Scientific)
714 selection medium. Cells were subsequently maintained in media supplemented with 1 µg/ml
715 puromycin.
716
717 **Lipid-based transfection of siRNA pools**
718 MEF SYF KO cells were reverse transfected with siRNAs (ON-TARGETplus SMARTpool,
719 Dharmacon Horizon Discovery) using lipofectamine RNAiMAX as per the manufacturer's
720 instructions (Thermo Fisher Scientific 13778030). Briefly, for each well of a 6-well plate, 6 µl
721 RNAiMAX was used to transfect 10 nM siRNA. After 24 hr, media was replaced with complete
722 growth medium and left to recover for another 24 hr prior to cell treatments and processing for
723 analysis.
724
725 **pNPP phosphatase activity assay**
726 Recombinant PTP domains were made up to 500 µl in assay buffer (50 mM Tris–HCl, pH 7.4,
727 150 mM NaCl, 5% [v/v] glycerol, 5 mM DTT) at 1 µM. PTPRK intracellular domain and 20 mM
728 pNPP substrate (NEB P0757S) (in assay buffer) were equilibrated to 30°C for 15 min in an
729 orbital shaking heat block at 500 RPM. To initiate reactions, 500 µl of 20 mM pNPP substrate
730 was added to PTP containing tubes (0.5 µM PTP and 10 mM pNPP final concentrations).
731 Reactions were carried out for 120 min at 30°C in an orbital shaking heat block at 500 RPM.
732 At each time point (0, 2, 5, 10, 15, 30, 60, 90 and 120 min), 100 µl of the total reaction was
733 transferred to a 96-well microplate well containing 50 µl 0.58 M NaOH, terminating the
734 reaction. After the final time point, absorbance of each sample was measured at 405 nm in a
735 Spectramax M5 plate reader (Molecular Devices). Product formation was calculated by
736 interpolation of absorbance values using a 4-nitrophenol standard curve of known
737 concentration.
738
739 **SDS-PAGE and immunoblotting**
740 Protein or cell lysate samples were resuspended in an appropriate volume of 5X SDS-PAGE
741 sample buffer (0.25 M Tris-HCl pH 6.8, 10% (w/v) SDS, 20% (v/v) glycerol, 0.1% (w/v)
742 bromophenol blue, 10% (v/v) β-mercaptoethanol) and incubated at 92°C for 10 min. Samples
743 were run on a 10% (v/v) SDS-polyacrylamide resolving gel with a 5% (v/v) SDS-PAGE
744 stacking gel and subjected to electrophoresis at 125 V for 1.5 h in 25 mM Tris, 190 mM glycine,
745 0.1% (w/v) SDS. Proteins were transferred onto 0.2 µm reinforced nitrocellulose membranes
746 (GE Healthcare) at 300 mA for 3 h at 4°C in 25 mM Tris, 190 mM glycine, 20% (v/v) methanol.
747 Membranes were briefly rinsed in TBS-T (20 mM Tris pH 7.6, 137 mM NaCl, 0.1% (v/v) Tween-
748 20) prior to incubation for 30 min in 5% (w/v) skimmed milk/TBS-T to block non-specific
749 antibody binding. The blocking solution was removed and membranes rinsed in TBS-T prior
750 to primary antibody incubation (overnight at 4°C). Membranes were then subjected to 3 × 10
751 min washes in TBS-T, prior to incubation with HRP-conjugated species-specific anti-IgG
752 antibodies (1 h at RT). Membranes were then subjected to 3 × 10 min washes in TBS-T, prior
753 to being incubated with combined EZ-ECL solution (Cytiva) and imaged using a G:BOX Chemi
754 XX6 (Syngene).
755
756 **Peroxiredoxin disulphide shift**

757 HEK293T cells were subjected to a pervanadate time course followed by incubation with PBS
758 with or without 10 µg/ml catalase (SLS #C3155) and 100 mM NEM for 15 mins at room
759 temperature. Catalase was added to the PBS 30 min prior to use with NEM added immediately
760 prior to use. Samples were lysed in 2 % SDS lysis buffer with and without 10 mM NEM.
761 Samples underwent immunoblotting on 12 % gels with either non-reducing or reducing
762 conditions and probed with PRDX1.
763
764 **PTPRK Flag overexpression, immunoprecipitation and pNPP assay**
765 Flag IP-phosphatase assays were performed as previously described (*74*). HEK293T (6 x10^6)
766 cells were plated in 10 cm^2 dishes, 24 h prior to transfection. 8 µg expression constructs for
767 3x FLAG tagged ICDs were transfected using 24 µl GeneJuice (Sigma) in 1 ml OPTIMEM
768 (Gibco) serum free media. Media was replaced 4 h post-transfection. For immunoprecipitation
769 (IP), cells were transferred to ice 48 h post transfection and washed twice with ice-cold 1X
770 phosphate buffered saline (PBS). Cells were lysed in ice-cold lysis buffer (50 mM Tris-HCl pH
771 7.4, 150 mM NaCl, 10 % [v/v] glycerol, 1 % [v/v] Triton X-100, 1 mM EDTA, 10 mM NaF, 1
772 mM PMSF, 1X-EDTA-free protease inhibitor) on ice for 30 mins with periodic agitation. Lysates
773 were collected and cleared by centrifugation at 14000 x g for 15 min at 4 °C and supernatants
774 were transferred to chilled tubes. Total protein concentration was quantified by bicinchoninic
775 acid (BCA) assay. Lysates were adjusted to a final concentration of 5 mM DTT to prevent air
776 oxidation. Equal amounts of total cell lysate for each sample (~2 mg) were combined with 50
777 µl (100 µl of 50 % slurry) of washed FLAG-M2 magnetic beads (Sigma Aldrich) in a total
778 volume of 1 ml made up in lysis buffer and incubated for 30 mins at 4 °C with rotation. Beads
779 were then collected on a magnetic stand and supernatants removed. Beads were then
780 resuspended and washed once with 1 ml lysis buffer and then four times with lysis buffer
781 containing 500 mM NaCl. For pNPP assays, IPs were then washed in 1 ml assay buffer (50
782 mM Tris-HCl pH 7.4, 150 mM NaCl, 5% [v/v] glycerol, 5 mM DTT] and then resuspended in
783 500 µl assay buffer. Samples were then subject to pNPP assays as described above. After
784 the assay beads were collected by magnet, washed in 1 ml TBS and resuspended in 1X SDS
785 PAGE sample buffer and incubated at 95°C for 5 mins. Beads were collected by magnet and
786 supernatants used for SDS-PAGE and immunoblot analysis.
787
788 **HyPer7 imaging and analysis**
789 U2OS cells expressing PM-HyPer7 were seeded on 35 mm glass bottom IBIDI dishes (81158)
790 prior to imaging and maintained at 37°C and 5% CO_2. Fluorescence excitation was measured
791 at 488 nm and 405 nm, and λem = 525 nm as described previously (*30*). Treatments were
792 prepared at 3x and added gently to the side of the culture dish after 1 min imaging. Images
793 were acquired using Total internal reflection fluorescence (TIRF) microscopy (Nikon Eclipse
794 STORM-TIRF microscope), using a 40x oil immersion objective. All image analysis was
795 conducted using ImageJ/FIJI. HyPer7 ratiometric images (λex=488/ λex=405) were false
796 coloured using mpl-Magma look-up table (purple to yellow). GraphPad Prism (Ver. 10) was
797 used for statistical analysis.
798
799 **HyPer7 and pervanadate reaction *in vitro***
800 Purified recombinant HyPer7 was buffer-exchanged into Ar-flushed 100 mM NaPOi, pH 7.4,
801 150 mM NaCl, 0.1 mM diethylene triamine penta-acetic acid (DTPA) using a 5 ml HiTrap
802 desalting column (GE Healthcare). The protein concentration was determined with the
803 Bradford reagent (Bio-Rad), using bovine serum albumin as a standard. The protein was
804 diluted to 2.8 µM and incubated with 0.1 mM DTT for 30 min at RT. Pervanadate, H_2O_2 and

805 catalase controls (subsequently referred to as “reactants”) were prepared at a 10x
806 concentration. HyPer7 (final concentration 2.5 μM) and the reactants were mixed in a quartz
807 cuvette, incubated for 1 min at RT and the fluorescence excitation spectrum was recorded
808 from λex = 350 nm to 505 nm with λem = 512 nm using a Cary Eclipse Fluorescence
809 Spectrophotometer (Agilent). The ratio of the two excitation maxima at 400 nm and 498.5 nm
810 was the final readout. GraphPad Prism (Ver. 10) was used for statistical analysis.
811
812 **Protein kinase assays**
813 Kinase assays were performed using nonradioactive real-time mobility shift-based microfluidic
814 assays, as described previously (*75*), in the presence of 2 mM of the appropriate fluorescent-
815 tagged peptide substrate (5-FAM-EGIYGVLFKKK-$CONH_2$) and 1 mM ATP (unless specified
816 otherwise). Pressure and voltage settings were adjusted manually to afford optimal separation
817 of phosphorylated and non-phosphorylated peptides. All assays were performed in 50 mM
818 HEPES (pH 7.4), 0.015% (v/v) Brij-35, and 5 mM $MgCl_2$, using 3 ng of SRC, and real-time or
819 end point peptide phosphorylation was determined using the ratio of the
820 phosphopeptide:peptide. Kinase activity in the presence of different redox reagents or inhibitor
821 compounds was quantified by monitoring the generation of phosphopeptide during the assay,
822 relative to controls, with phosphate incorporation into the peptide generally limited to <20% to
823 prevent ATP depletion and maintain assay linearity. The effects of variable exposure times on
824 kinase activity were monitored by preincubating SRC and redox reagent for 10, 60 or 120 mins
825 at room temperature (RT), and then initiating substrate phosphorylation with the addition of
826 ATP and peptide substrate. Relative changes of SRC activity in the presence of increasing
827 concentrations of pervanadate were monitored in real time over 4 h using 20 μM peptide
828 substrate. The rate of substrate phosphorylation at each time point was calculated as pmol
829 phosphate incorporation per min and plotted as a function of total assay time. Counter screen
830 assays using 50 ng Aurora A kinase were performed as for SRC.
831
832 **Differential alkylation in cell lysates**
833 Differential alkylation methodology was performed as previously described (*76*). HEK293T
834 cells were plated at 2 $x10^6$ per 10 cm^2 dish until full confluency followed by PV treatments.
835 Cells were washed twice in ice-cold PBS followed by harvesting into pH 7.0 lysis buffer [30
836 mM Tris-HCL (pH 7), 120 mM NaCl, 2 mM EDTA, 2 mM KCl, 10 % (v/v) glycerol, 1 % (v/v)
837 triton, 1 % SDS (v/v), 5 mM NaF, 1X EDTA-free protease inhibitor tablet cocktail (Roche;
838 1836170001) and PhosSTOP tablets (Roche; 4906845001)] containing NEM (Sigma; E3876)
839 5 mM for alkylation. Lysates were then sonicated and incubated on ice for 20 min in the dark
840 to enable NEM alkylation, followed by centrifugation at 13000 x g to pre-clear the lysate.
841 During this incubation, Zeba™ spin desalting columns (Thermo Fisher Scientific; 89882) were
842 equilibrated with lysis buffer pH 8.0 following the manufacturer’s instructions. 0.5 mg protein
843 per sample was buffer exchanged by filtering through three Zeba™ spin columns per sample
844 to remove excess NEM. 50 mM TCEP (Merck; 646547) was added to each sample followed
845 by incubation at room temp for 30 mins to enable sample reduction. Samples were then filtered
846 through three pH 8.0 lysis buffer equilibrated Zeba™ columns per sample to remove excess
847 TCEP. Finally, samples were incubated with 10 mM EZ-Link™ Iodoacetyl-PEG2-Biotin
848 (Thermo Fisher Scientific; 21334) for 90 mins at RT in the dark, followed by buffer exchange
849 through three equilibrated Zeba™ spin columns to remove excess alkylating agent. Lysates
850 were then subjected to streptavidin enrichment using the following method. Protein
851 concentration was measured again for each sample using BCA assay and 400 μg each
852 sample was subject to pull-down. 10 % lysate was removed and added to sample buffer for

853 input sample. Remaining lysate was incubated with 50 µl neutravidin beads (Pierce; 29202)
854 rotating for 2 h at 4°C. Equivalent of 10 % starting lysate concentration was removed for
855 supernatant sample and added to sample buffer. The remaining beads were washed 4x with
856 RIPA buffer [50 mM Tris-HCl, pH 7.4, 1% (v/v) Triton, 1% Na deoxycholate, 0.1% SDS, 150
857 mM NaCl, 1 mM EDTA] followed by elution in 5x sample buffer with 25 mM biotin (Merck;
858 B4639) with incubation at 95°C for 10 mins. Input, supernatant and pull-down samples then
859 underwent analysis by immunoblotting.
860
861 **SRC affinity precipitation from HEK293T cells**
862 Affinity precipitation experiments used HEK293T cells transfected using a 3:1
863 polyethyleneimine [average Mw (weight-average molecular weight), ~25,000 Da; Sigma-
864 Aldrich] to DNA ratio (30:10 mg, for a single 10 cm^2 culture dish). Proteins were harvested 48
865 h post transfection using a lysis buffer containing 50 mM Tris-HCl (pH 7.4), 150 mM NaCl,
866 0.1% (v/v) Triton X-100, and 5% (v/v) glycerol and supplemented with a protease inhibitor
867 cocktail tablet and a phosphatase inhibitor tablet (Roche). Lysates were briefly sonicated on
868 ice and clarified by centrifuged at 20,817g for 20 min at 4°C, and the resulting supernatants
869 were incubated with Strep-TactinXT 4Flow affinity resin (IBA Lifesciences) for 1 h with gentle
870 end over end mixing at 4°C. Beads containing bound protein were collected and washed three
871 times in 50 mM tris-HCl (pH 7.4) and 500 mM NaCl and then equilibrated in storage buffer [50
872 mM Tris-HCl (pH 7.4), 100 mM NaCl, and 5% (v/v) glycerol]. The purified kinases were then
873 proteolytically eluted from the beads over a 1 h period using 3C protease (0.5 mg) at 4°C with
874 gentle agitation and then assayed using real-time microfluidic peptide assay as described
875 above. For MS-dependent detection of cysteine modifications, HEK293T cells were treated
876 with pervanadate or H_2O_2 for 30 mins, and protein harvested in 50 mM Tris-HCl (pH 6.5), 150
877 mM NaCl, 0.1% (v/v) Triton X-100, and 5% (v/v) glycerol supplemented with a protease and
878 phosphatase inhibitor tablets (Roche), and 100 mM iodoacetamide to alkylate thiols. After brief
879 sonication, lysates were incubated in the dark for 1 h at 4°C, clarified by centrifugation and
880 affinity purified as above.
881
882 **Identification of affinity enriched SRC cysteine oxidation state using mass**
883 **spectrometry**
884 Affinity purified SRC preparations were diluted to 180 µl in 100 mM ammonium bicarbonate
885 pH 8.0 and reduced and alkylated with dithiothreitol and iodoacetamide, as previously
886 described by (*77*). Samples were subject to SP3-bead digestion as described by (*78*) with the
887 adaptions of: using 100 mM ammonium bicarbonate pH 8.0, 0.5 µg Trypsin gold (Promega)
888 and post-digest bead washing in 1% (w/v) Rapigest (Waters). Once supernatants were
889 combined, samples were acidified by addition of a final concentration of 0.5% TFA and
890 incubated for 30 min each at 37 °C with 600 rpm shaking and on ice. Samples were centrifuged
891 at 13000 x g for 10 min at 4 °C and cleared supernatant collected into fresh tubes prior to
892 vacuum centrifugation. Dried peptides were solubilized in 20 µl of 3% (v/v) acetonitrile and
893 0.1% (v/v) TFA in water, sonicated for 10 minutes, and centrifuged at 13000 x g for 15 min at
894 4 °C prior to reversed-phase HPLC separation using an Ultimate3000 nano system (Dionex)
895 over a 60 min gradient, as described by (*79*). All data acquisition was performed using a
896 Thermo QExactive HF mass spectrometer (Thermo Fisher Scientific), with higher-energy C-
897 trap dissociation (HCD) fragmentation set at 29% normalized collision energy for 2+ to 5+
898 charge states. MS1 spectra were acquired in the Orbitrap (60K resolution at 200 m/z) over a
899 m/z range of 350 to 2000, AGC target = 3e6, maximum injection time = 100 ms, with an
900 intensity threshold for fragmentation of 1e3. MS2 spectra were acquired in the Orbitrap (30K

901 resolution at 200 m/z), maximum injection time = 45 ms, AGC target = 1e5 with a 20 s dynamic
902 exclusion window applied with a 10-ppm tolerance. Data was analyzed using Proteome
903 Discoverer 2.4 (Thermo Fisher Scientific) in conjunction with MASCOT (*80*); searching the
904 UniProt Human Reviewed database (updated weekly, accessed March 2022) with constant
905 modifications = carbamidomethyl (C), variable modifications = oxidation (M), phosphorylation
906 (ST), trioxidation (C), instrument type = electrospray ionization–Fourier-transform ion cyclotron
907 resonance (ESI-FTICR), MS1 mass tolerance = 10 ppm, MS2 mass tolerance = 0.01 Da with
908 the ptmRS node active. Label free quantification was performed using the Minora feature
909 detector node, calculating the area under the curve for m/z values, total protein abundance
910 was determined using the HI3 method (*81*). For cysteine trioxidation-containing peptides
911 identified in at least 3 replicates, peptide abundance was normalized against the calculated
912 total protein abundance to account for potential protein load variability during analysis prior to
913 normalization against untreated control. For the best MASCOT scoring PSM of a C188-
914 trioxidation containing peptide, the spectrum was extracted in *.mgf format from the raw file
915 and imported into a custom R script for re-drawing and manual annotation.
916
917 **Differential scanning fluorimetry**
918 Thermal shift assays were performed using a StepOnePlus real-time polymerase chain
919 reaction (PCR) machine (Life Technologies) using SYPRO Orange dye (Invitrogen) and
920 thermal ramping (0.3°C in step intervals between 25°C and 94°C). Recombinant SRC proteins
921 were assayed at a final concentration of 2.5 mM in 50 mM tris-HCl (pH 7.4) and 100 mM NaCl
922 in the presence or absence of the indicated concentrations of ATP, H_2O_2, DTT, orthovanadate,
923 pervanadate or Dasatinib [final dimethyl sulfoxide (DMSO) concentration no higher than 4%
924 (v/v)] as described previously (*75*). Normalized data were processed using the Boltzmann
925 equation to generate sigmoidal denaturation curves, and average Tm/ΔTm values were
926 calculated as previously described (*82*) using GraphPad Prism software.
927
928 **Hydrogen-Deuterium exchange mass spectrometry**
929 A preincubation was performed by adding to a concentrated SRC sample (57 μM SRC in 50
930 mM Tris pH 7.5, 150 mM NaCl) a 4.5 mM PV solution to yield a final solution of 5 μM SRC (20
931 mM Hepes pH 7, 150 mM NaCl) in presence of 0.5 mM or 2.5 mM of PV. Samples were
932 incubated for 15 minutes at room temperature and then exposed for different deuteration times
933 (3 seconds on ice, 3, 30, 300 and 3000 seconds at room temperature) to a deuterated buffer:
934 50 mM Tris pH 7.5, 150 mM NaCl, with D_2O at a final concentration of 90% (Thermo Fisher
935 Scientific, 166300100) to yield a final solution that was 0.5 μM of SRC in absence/presence
936 of 0.05 mM or 0.25 mM of PV. Triplicate samples were aliquoted for each deuteration
937 timepoint. Exchange reactions were quenched in 2 M Guanidine-Hydrochloride, 100 mM
938 Glycine, formic acid (Fisher Chemical, 10596814), LC-MS grade water (Romil, H949), pH 2.3
939 (final pH was 2.5). Samples were then flash-frozen in liquid nitrogen immediately and stored
940 at -80 °C until analysis. Prior to LC-MS analysis, samples were quickly thawed and injected
941 on a HDX sample manager coupled to an Acquity ultra performance liquid chromatography
942 (UPLC) M-Class system (Waters) set at 0.1 °C. Samples were then digested at 15 °C using a
943 20 mm x 2.0 mm home-made pepsin column (Pepsin from Thermo Scientific, 20343 and
944 hardware from Upchurch Scientific, C130-B) and loaded on a UPLC pre-column (Acquity
945 UPLC BEH C18 VanGuard pre-column, 2.1 mm I.D. × 5 mm, 1.7 μm particle diameter, Waters,
946 186003975) for 2 min at 100 μL/min. Digested peptides were then eluted from the pre-column
947 onto an Acquity UPLC BEH C18 column (1.0 mm I.D. × 100 mm, 1.7 μm particle diameter,
948 Waters, 186002346) using a 5-43% gradient of Acetonitrile (Romil, H050), 0.1% formic acid

949 over 12 min. MS data acquisition was done on a Synapt G2Si-HDMS (Waters) with positive
950 electrospray ionization, using $HDMS^E$ acquisition mode over a *m*/*z* range of 50–2000 and a
951 100 fmol.μL^{-1} Glu-FibrinoPeptide solution was used for lock-mass correction and calibration.
952 The following parameters were used during the acquisition: capillary voltage, 3 kV; sampling
953 cone voltage, 40 V; source temperature, 90°C; desolvation gas, 150°C and 650 $L.h^{-1}$; scan
954 time, 0.3 s; trap collision energy ramp, 20–45 eV. Peptide identification was performed using
955 ProteinLynx Global Server 3.0.1 (Waters) with a home-made protein sequence library
956 containing SRC and pepsin sequences, with peptide and fragment tolerances set
957 automatically by PLGS. Deuterium uptakes for all identified peptides were then filtered and
958 validated manually using DynamX 3.0 (Waters) as follows: only peptides identified with a
959 minimum fragment per amino acid of 0.2, a minimum intensity of 10^3, a length between 5 and
960 25 residues, a minimum PLGS score of 6.62 and a MH^+ tolerance of 5 ppm were kept. An
961 initial automated spectral processing step was conducted by DynamX followed by a manual
962 inspection of individual peptides for sufficient quality where only one charge state per peptide
963 was kept. Deuterium uptake is not corrected for back-exchange and is reported as relative
964 values. HDX-MS results were statistically validated using an in-house program
965 (Archaeopteryx), where the t-statistic threshold was set to 0.05. Only statistically significant
966 peptides showing a difference greater than 0.25 Da and 2% for at least two timepoints were
967 kept. HDX-MS results were illustrated on SRC open and closed conformations (PDB: 2SRC
968 and 1Y57 respectively) using PyMOL 2.5.4 (www.pymol.org).
969
970 **AlphaFold3 modeling**
971 SRC SH2 and C-terminal pTyr complexes were modelled from sequence using AlphaFold3
972 through its public web server (https://www.alphafoldserver.com). Standard AlphaFold
973 procedures were followed, and the outputs were manually inspected to confirm the correct
974 orientation of the SH2 domain bound to peptide. Post-translational modifications were added
975 using the PTMs function on the selected residues. For each complex, five models were
976 generated, and their confidence metrics were evaluated using the AlphaFold3 ranking scores.
977 The highest-ranking model, determined by its pLDDT score, was selected for further analysis.
978 Structural representations were prepared using UCSF Chimera, and alignment was performed
979 using MatchMaker in Chimera X.
980
981 **Isothermal Titration Calorimetry**
982 ITC experiment was measured by MicroCal PEAQ-ITC Automated at 25℃. After treatment,
983 SRC SH2 domains and peptides were buffer exchanged into fresh experimental buffer using
984 ultrafiltration prior to titrations. ITC experiments were performed by stepwise titration of the
985 peptides (400 μM) into an adiabatic cell containing SRC SH2 (40 μM), and the heat energy
986 change accompanying the reaction was detected upon each injection by comparison with a
987 reference cell. The stoichiometry of binding (n) was between 0.84 and 1.1 for all experiments.
988 Protein solution was placed in the 380 μl calorimeter cell and stirred at 750 rpm to ensure
989 rapid mixing, and 2 μl aliquots of the peptides were injected with a 120 s interval between each
990 injection until saturation. The heat changes were integrated after subtracting values obtained
991 when peptides were titrated into buffer, data were analyzed with the MicroCal PEAQ-ITC
992 software.
993
994 **Cell counting and Incucyte® imaging**
995 MEFs were plated on fibronectin (Roche #10838039001) 5 μg/cm^2 coated 6-well plates at 0.2
996 x10^6 and grown over 6 days with a media change on day 3. On daily intervals, one well was

997 trypsinized, resuspended in normal growth medium and counted with trypan blue using the
998 countess cell counter (Invitrogen) for the manual growth curves. For live imaging, MEFs were
999 plated on fibronectin (Roche; 10838039001) 5 µg/cm^2 coated CytoOne 96-well plates at 2.5
1000 x10^5 cells per well. The following day, the plate was transferred to an Incucyte® S3 live cell
1001 imaging and analysis system (Sartorious; IC70682) and 4 regions were imaged per well every
1002 2 h for 6 days. Media was refreshed on day 3.
1003
1004 **Immunofluorescence microscopy**
1005 Cells were plated on fibronectin (Roche #10838039001) 5 µg/cm^2 coated coverslips at 0.2
1006 x10^6 and let to grow for 6 days with a media change on day 3. Then fixed using 4%
1007 paraformaldehyde in PBS for 10 min. The cells were then permeabilized in 0.5% Triton X-100
1008 and 3% BSA in PBS for 2 min and blocked in 0.2% Triton X-100 and 3% BSA in PBS (blocking
1009 buffer) for 1 h. They were stained using Alexa Fluor™ Plus 647 Phalloidin (1:200) and Hoechst
1010 (1:2000) for 1 h then washed 3 times in blocking buffer for 1 h. Images were taken using and
1011 Leica Stellaris 8 with a 40X objective and 1.5 zoom. The nucleus of 6 different fields per
1012 condition were counted.
1013
1014 **Ethical Statement**
1015 All animal experiments at The Babraham Institute were reviewed and approved by The Animal
1016 Welfare and Ethics Review Body and performed under Home Office Project license
1017 PP4624082.
1018
1019 **Supplementary materials:**
1020 Figs. S1 to S6
1021 Movies S1-S6
1022 Table S1.
1023
1024 **References**

1025 1. T. Hunter, Tyrosine phosphorylation: thirty years and counting. *Curr Opin Cell Biol* **21**, 140-
1026 146 (2009); published online EpubApr (10.1016/j.ceb.2009.01.028).
1027 2. J. Baselga, Targeting Tyrosine Kinases in Cancer: The Second Wave. *Science* **312**, 1175-
1028 1178 (2006); published online Epub2006/05/26 (10.1126/science.1125951).
1029 3. A. Östman, C. Hellberg, F. D. Böhmer, Protein-tyrosine phosphatases and cancer. *Nature*
1030 *Reviews Cancer* **6**, 307 (2006); published online Epub04/01/online (10.1038/nrc1837
1031 https://www.nature.com/articles/nrc1837#supplementary-information).
1032 4. C. K. Baumgartner, H. Ebrahimi-Nik, A. Iracheta-Vellve, K. M. Hamel, K. E. Olander, T. G.
1033 R. Davis, K. A. McGuire, G. T. Halvorsen, O. I. Avila, C. H. Patel, S. Y. Kim, A. V.
1034 Kammula, A. J. Muscato, K. Halliwill, P. Geda, K. L. Klinge, Z. Xiong, R. Duggan, L. Mu,
1035 M. D. Yeary, J. C. Patti, T. M. Balon, R. Mathew, C. Backus, D. E. Kennedy, A. Chen, K.
1036 Longenecker, J. T. Klahn, C. L. Hrusch, N. Krishnan, C. W. Hutchins, J. P. Dunning, M.
1037 Bulic, P. Tiwari, K. J. Colvin, C. L. Chuong, I. C. Kohnle, M. G. Rees, A. Boghossian, M.
1038 Ronan, J. A. Roth, M.-J. Wu, J. S. M. T. Suermondt, N. H. Knudsen, C. K. Cheruiyot, D. R.
1039 Sen, G. K. Griffin, T. R. Golub, N. El-Bardeesy, J. H. Decker, Y. Yang, M. Guffroy, S.
1040 Fossey, P. Trusk, I.-M. Sun, Y. Liu, W. Qiu, Q. Sun, M. N. Paddock, E. P. Farney, M. A.
1041 Matulenko, C. Beauregard, J. M. Frost, K. B. Yates, P. R. Kym, R. T. Manguso, The
1042 PTPN2/PTPN1 inhibitor ABBV-CLS-484 unleashes potent anti-tumour immunity. *Nature*
1043 **622**, 850-862 (2023); published online Epub2023/10/01 (10.1038/s41586-023-06575-7).
1044 5. Y. N. Chen, M. J. LaMarche, H. M. Chan, P. Fekkes, J. Garcia-Fortanet, M. G. Acker, B.
1045 Antonakos, C. H. Chen, Z. Chen, V. G. Cooke, J. R. Dobson, Z. Deng, F. Fei, B. Firestone,
1046 M. Fodor, C. Fridrich, H. Gao, D. Grunenfelder, H. X. Hao, J. Jacob, S. Ho, K. Hsiao, Z. B.

Kang, R. Karki, M. Kato, J. Larrow, L. R. La Bonte, F. Lenoir, G. Liu, S. Liu, D. Majumdar, M. J. Meyer, M. Palermo, L. Perez, M. Pu, E. Price, C. Quinn, S. Shakya, M. D. Shultz, J. Slisz, K. Venkatesan, P. Wang, M. Warmuth, S. Williams, G. Yang, J. Yuan, J. H. Zhang, P. Zhu, T. Ramsey, N. J. Keen, W. R. Sellers, T. Stams, P. D. Fortin, Allosteric inhibition of SHP2 phosphatase inhibits cancers driven by receptor tyrosine kinases. *Nature* **535**, 148-152 (2016); published online EpubJul 7 (10.1038/nature18621).

6. G. Huyer, S. Liu, J. Kelly, J. Moffat, P. Payette, B. Kennedy, G. Tsaprailis, M. J. Gresser, C. Ramachandran, Mechanism of Inhibition of Protein-tyrosine Phosphatases by Vanadate and Pervanadate. *Journal of Biological Chemistry* **272**, 843-851 (1997); published online EpubJanuary 10, 1997 (10.1074/jbc.272.2.843).

7. I. G. Fantus, S. Kadota, G. Deragon, B. Foster, B. I. Posner, Pervanadate [peroxide(s) of vanadate] mimics insulin action in rat adipocytes via activation of the insulin receptor tyrosine kinase. *Biochemistry* **28**, 8864-8871 (1989); published online EpubOct 31 (10.1021/bi00448a027).

8. E. Irving, A. W. Stoker, Vanadium Compounds as PTP Inhibitors. *Molecules* **22**, (2017); published online EpubDec 19 (10.3390/molecules22122269).

9. B. I. Posner, R. Faure, J. W. Burgess, A. P. Bevan, D. Lachance, G. Zhang-Sun, I. G. Fantus, J. B. Ng, D. A. Hall, B. S. Lum, et al., Peroxovanadium compounds. A new class of potent phosphotyrosine phosphatase inhibitors which are insulin mimetics. *J Biol Chem* **269**, 4596-4604 (1994); published online EpubFeb 11 (

10. C. Blanchetot, M. Chagnon, N. Dubé, M. Hallé, M. L. Tremblay, Substrate-trapping techniques in the identification of cellular PTP targets. *Methods* **35**, 44-53 (2005); published online EpubJan (10.1016/j.ymeth.2004.07.007).

11. R. Karisch, M. Fernandez, P. Taylor, C. Virtanen, J. R. St-Germain, L. L. Jin, I. S. Harris, J. Mori, T. W. Mak, Y. A. Senis, A. Ostman, M. F. Moran, B. G. Neel, Global proteomic assessment of the classical protein-tyrosine phosphatome and "Redoxome". *Cell* **146**, 826-840 (2011); published online EpubSep 2 (10.1016/j.cell.2011.07.020).

12. I. Boulven, P. Robin, C. Desmyter, S. Harbon, D. Leiber, Differential involvement of Src family kinases in pervanadate-mediated responses in rat myometrial cells. *Cellular Signalling* **14**, 341-349 (2002); published online Epub2002/04/01/ (https://doi.org/10.1016/S0898-6568(01)00269-8).

13. A. Shisheva, Y. Shechter, Mechanism of pervanadate stimulation and potentiation of insulin-activated glucose transport in rat adipocytes: dissociation from vanadate effect. *Endocrinology* **133**, 1562-1568 (1993)10.1210/endo.133.4.8404595).

14. S. J. Davis, P. A. van der Merwe, The kinetic-segregation model: TCR triggering and beyond. *Nature Immunology* **7**, 803 (2006); published online Epub07/19/online (10.1038/ni1369 https://www.nature.com/articles/ni1369#supplementary-information).

15. V. Imbert, J. F. Peyron, D. Farahi Far, B. Mari, P. Auberger, B. Rossi, Induction of tyrosine phosphorylation and T-cell activation by vanadate peroxide, an inhibitor of protein tyrosine phosphatases. *Biochem J* **297 (Pt 1)**, 163-173 (1994); published online EpubJan 1 (10.1042/bj2970163).

16. J. P. Secrist, L. A. Burns, L. Karnitz, G. A. Koretzky, R. T. Abraham, Stimulatory effects of the protein tyrosine phosphatase inhibitor, pervanadate, on T-cell activation events. *J Biol Chem* **268**, 5886-5893 (1993); published online EpubMar 15 (

17. A. H. Courtney, J. F. Amacher, T. A. Kadlecek, M. N. Mollenauer, B. B. Au-Yeung, J. Kuriyan, A. Weiss, A Phosphosite within the SH2 Domain of Lck Regulates Its Activation by CD45. *Mol Cell* **67**, 498-511.e496 (2017); published online EpubAug 3 (10.1016/j.molcel.2017.06.024).

18. A. H. Courtney, A. A. Shvets, W. Lu, G. Griffante, M. Mollenauer, V. Horkova, W.-L. Lo, S. Yu, O. Stepanek, A. K. Chakraborty, A. Weiss, CD45 functions as a signaling gatekeeper in T cells. *Science Signaling* **12**, eaaw8151 (2019)10.1126/scisignal.aaw8151).

19. E. Giannoni, F. Buricchi, G. Raugei, G. Ramponi, P. Chiarugi, Intracellular Reactive Oxygen Species Activate Src Tyrosine Kinase during Cell Adhesion and Anchorage-Dependent Cell Growth. *Molecular and Cellular Biology* **25**, 6391-6403 (2005); published online Epub12/27/received

02/16/revised
05/04/accepted (10.1128/MCB.25.15.6391-6403.2005).
20. D. E. Heppner, Structural insights into redox-active cysteine residues of the Src family kinases. *Redox Biol* **41**, 101934 (2021); published online EpubMay (10.1016/j.redox.2021.101934).
21. D. E. Heppner, C. M. Dustin, C. Liao, M. Hristova, C. Veith, A. C. Little, B. A. Ahlers, S. L. White, B. Deng, Y. W. Lam, J. Li, A. van der Vliet, Direct cysteine sulfenylation drives activation of the Src kinase. *Nat Commun* **9**, 4522 (2018); published online EpubOct 30 (10.1038/s41467-018-06790-1).
22. T. H. Truong, P. M. Ung, P. B. Palde, C. E. Paulsen, A. Schlessinger, K. S. Carroll, Molecular Basis for Redox Activation of Epidermal Growth Factor Receptor Kinase. *Cell Chem Biol* **23**, 837-848 (2016); published online EpubJul 21 (10.1016/j.chembiol.2016.05.017).
23. S. K. Yoo, T. W. Starnes, Q. Deng, A. Huttenlocher, Lyn is a redox sensor that mediates leukocyte wound attraction in vivo. *Nature* **480**, 109-112 (2011); published online Epub2011/12/01 (10.1038/nature10632).
24. H. Zhang, K. J. A. Davies, H. J. Forman, TGFβ1 rapidly activates Src through a non-canonical redox signaling mechanism. *Archives of Biochemistry and Biophysics* **568**, 1-7 (2015); published online Epub2015/02/15/ (https://doi.org/10.1016/j.abb.2015.01.001).
25. S.-O. Mikalsen, O. Kaalhus, Properties of Pervanadate and Permolybdate: CONNEXIN43, PHOSPHATASE INHIBITION, AND THIOL REACTIVITY AS MODEL SYSTEMS *. *Journal of Biological Chemistry* **273**, 10036-10045 (1998)10.1074/jbc.273.16.10036).
26. G.-Z. Tao, Q. Zhou, P. Strnad, M. R. Salemi, Y. M. Lee, M. B. Omary, Human Ran Cysteine 112 Oxidation by Pervanadate Regulates Its Binding to Keratins. *Journal of Biological Chemistry* **280**, 12162-12167 (2005).
27. V. A. Alcántara-Mejía, J. J. Rodríguez-Mercado, R. A. Mateos-Nava, L. Álvarez-Barrera, E. Santiago-Osorio, E. Bonilla-González, M. A. Altamirano-Lozano, Oxidative damage and cell cycle delay induced by vanadium(III) in human peripheral blood cells. *Toxicology Reports* **13**, 101695 (2024); published online Epub2024/12/01/ (https://doi.org/10.1016/j.toxrep.2024.101695).
28. R. Faure, G. Baquiran, J. J. Bergeron, B. I. Posner, The dephosphorylation of insulin and epidermal growth factor receptors. Role of endosome-associated phosphotyrosine phosphatase(s). *Journal of Biological Chemistry* **267**, 11215-11221 (1992); published online Epub1992/06/05/ (https://doi.org/10.1016/S0021-9258(19)49898-0).
29. P. Kritsiligkou, T. K. Shen, T. P. Dick, A comparison of Prx- and OxyR-based H₂O₂ probes expressed in S. cerevisiae. *Journal of Biological Chemistry* **297**, (2021)10.1016/j.jbc.2021.100866).
30. V. V. Pak, D. Ezeriņa, O. G. Lyublinskaya, B. Pedre, P. A. Tyurin-Kuzmin, N. M. Mishina, M. Thauvin, D. Young, K. Wahni, S. A. Martínez Gache, A. D. Demidovich, Y. G. Ermakova, Y. D. Maslova, A. G. Shokhina, E. Eroglu, D. S. Bilan, I. Bogeski, T. Michel, S. Vriz, J. Messens, V. V. Belousov, Ultrasensitive Genetically Encoded Indicator for Hydrogen Peroxide Identifies Roles for the Oxidant in Cell Migration and Mitochondrial Function. *Cell Metabolism* **31**, 642-653.e646 (2020)10.1016/j.cmet.2020.02.003).
31. A. Zhuravlev, D. Ezeriņa, J. Ivanova, N. Guriev, N. Pugovkina, A. Shatrova, N. Aksenov, J. Messens, O. Lyublinskaya, HyPer as a tool to determine the reductive activity in cellular compartments. *Redox Biology* **70**, 103058 (2024); published online Epub2024/04/01/ (https://doi.org/10.1016/j.redox.2024.103058).
32. H. A. Woo, S. H. Yim, D. H. Shin, D. Kang, D. Y. Yu, S. G. Rhee, Inactivation of peroxiredoxin I by phosphorylation allows localized H(2)O(2) accumulation for cell signaling. *Cell* **140**, 517-528 (2010); published online EpubFeb 19 (10.1016/j.cell.2010.01.009).
33. C. Fan, Q. Li, D. Ross, J. F. Engelhardt, Tyrosine Phosphorylation of IκBα Activates NFκB through a Redox-regulated and c-Src-dependent Mechanism Following Hypoxia/Reoxygenation*. *Journal of Biological Chemistry* **278**, 2072-2080 (2003); published online Epub2003/01/17/ (https://doi.org/10.1074/jbc.M206718200).

34. J. B. Bertoldo, T. Rodrigues, L. Dunsmore, F. A. Aprile, M. C. Marques, L. A. Rosado, O. Boutureira, T. B. Steinbrecher, W. Sherman, F. Corzana, H. Terenzi, G. J. L. Bernardes, A Water-Bridged Cysteine-Cysteine Redox Regulation Mechanism in Bacterial Protein Tyrosine Phosphatases. *Chem* **3**, 665-677 (2017); published online EpubOct 12 (10.1016/j.chempr.2017.07.009).
35. S. R. Hubbard, Src autoinhibition: let us count the ways. *Nat Struct Biol* **6**, 711-714 (1999); published online EpubAug (10.1038/11468).
36. I. Moarefi, M. LaFevre-Bernt, F. Sicheri, M. Huse, C. H. Lee, J. Kuriyan, W. T. Miller, Activation of the Src-family tyrosine kinase Hck by SH3 domain displacement. *Nature* **385**, 650-653 (1997); published online EpubFeb 13 (10.1038/385650a0).
37. W. Xu, A. Doshi, M. Lei, M. J. Eck, S. C. Harrison, Crystal Structures of c-Src Reveal Features of Its Autoinhibitory Mechanism. *Molecular Cell* **3**, 629-638 (1999); published online Epub1999/05/01/ (https://doi.org/10.1016/S1097-2765(00)80356-1).
38. S. W. Cowan-Jacob, G. Fendrich, P. W. Manley, W. Jahnke, D. Fabbro, J. Liebetanz, T. Meyer, The crystal structure of a c-Src complex in an active conformation suggests possible steps in c-Src activation. *Structure* **13**, 861-871 (2005); published online EpubJun (10.1016/j.str.2005.03.012).
39. T. J. Boggon, M. J. Eck, Structure and regulation of Src family kinases. *Oncogene* **23**, 7918-7927 (2004); published online EpubOct 18 (10.1038/sj.onc.1208081).
40. Y. Meng, B. Roux, Computational study of the W260A activating mutant of Src tyrosine kinase. *Protein Sci* **25**, 219-230 (2016); published online EpubJan (10.1002/pro.2731).
41. Y. Meng, B. Roux, Locking the active conformation of c-Src kinase through the phosphorylation of the activation loop. *J Mol Biol* **426**, 423-435 (2014); published online EpubJan 23 (10.1016/j.jmb.2013.10.001).
42. J. Abramson, J. Adler, J. Dunger, R. Evans, T. Green, A. Pritzel, O. Ronneberger, L. Willmore, A. J. Ballard, J. Bambrick, S. W. Bodenstein, D. A. Evans, C.-C. Hung, M. O'Neill, D. Reiman, K. Tunyasuvunakool, Z. Wu, A. Žemgulytė, E. Arvaniti, C. Beattie, O. Bertolli, A. Bridgland, A. Cherepanov, M. Congreve, A. I. Cowen-Rivers, A. Cowie, M. Figurnov, F. B. Fuchs, H. Gladman, R. Jain, Y. A. Khan, C. M. R. Low, K. Perlin, A. Potapenko, P. Savy, S. Singh, A. Stecula, A. Thillaisundaram, C. Tong, S. Yakneen, E. D. Zhong, M. Zielinski, A. Žídek, V. Bapst, P. Kohli, M. Jaderberg, D. Hassabis, J. M. Jumper, Accurate structure prediction of biomolecular interactions with AlphaFold 3. *Nature* **630**, 493-500 (2024); published online Epub2024/06/01 (10.1038/s41586-024-07487-w).
43. G. Payne, L. A. Stolz, D. Pei, H. Band, S. E. Shoelson, C. T. Walsh, The phosphopeptide-binding specificity of Src family SH2 domains. *Chem Biol* **1**, 99-105 (1994); published online EpubOct (10.1016/1074-5521(94)90047-7).
44. J. M. Bradshaw, V. Mitaxov, G. Waksman, Investigation of phosphotyrosine recognition by the SH2 domain of the Src kinase11Edited by P. E. Wright. *Journal of Molecular Biology* **293**, 971-985 (1999); published online Epub1999/11/05/ (https://doi.org/10.1006/jmbi.1999.3190).
45. M. Morra, M. Simarro-Grande, M. Martin, A. S.-I. Chen, A. Lanyi, O. Silander, S. Calpe, J. Davis, T. Pawson, M. J. Eck, J. Sumegi, P. Engel, S.-C. Li, C. Terhorst, Characterization of SH2D1A Missense Mutations Identified in X-linked Lymphoproliferative Disease Patients*. *Journal of Biological Chemistry* **276**, 36809-36816 (2001); published online Epub2001/09/28/ (https://doi.org/10.1074/jbc.M101305200).
46. D. Bajusz, G. Pándy-Szekeres, Á. Takács, E. D. de Araujo, G. M. Keserű, SH2db, an information system for the SH2 domain. *Nucleic Acids Res* **51**, W542-W552 (2023)10.1093/nar/gkad420).
47. P. R. Visperas, J. A. Winger, T. M. Horton, N. H. Shah, D. J. Aum, A. Tao, T. Barros, Q. Yan, C. G. Wilson, M. R. Arkin, A. Weiss, J. Kuriyan, Modification by covalent reaction or oxidation of cysteine residues in the tandem-SH2 domains of ZAP-70 and Syk can block phosphopeptide binding. *Biochem J* **465**, 149-161 (2015); published online EpubJan 1 (10.1042/bj20140793).
48. L. Koudelková, A. C. Pataki, O. Tolde, V. Pavlik, M. Nobis, J. Gemperle, K. Anderson, J. Brábek, D. Rosel, Novel FRET-Based Src Biosensor Reveals Mechanisms of Src Activation

and Its Dynamics in Focal Adhesions. *Cell Chem Biol* **26**, 255-268.e254 (2019); published online EpubFeb 21 (10.1016/j.chembiol.2018.10.024).

49. L. E. Arias-Romero, S. Saha, O. Villamar-Cruz, S.-C. Yip, S. P. Ethier, Z.-Y. Zhang, J. Chernoff, Activation of Src by Protein Tyrosine Phosphatase 1B Is Required for ErbB2 Transformation of Human Breast Epithelial Cells. *Cancer Research* **69**, 4582-4588 (2009)10.1158/0008-5472.CAN-08-4001).

50. M. P. Playford, M. D. Schaller, The interplay between Src and integrins in normal and tumor biology. *Oncogene* **23**, 7928-7946 (2004); published online Epub2004/10/01 (10.1038/sj.onc.1208080).

51. X. M. Zheng, Y. Wang, C. J. Fallen, Cell transformation and activation of pp60c-src by overexpression of a protein tyrosine phosphatase. *Nature* **359**, 336-339 (1992); published online Epub1992/09/01 (10.1038/359336a0).

52. C. M. Dustin, A. Habibovic, M. Hristova, C. Schiffers, C. R. Morris, M. J. Lin, R. A. Bauer, D. E. Heppner, N. Daphtary, M. Aliyeva, A. van der Vliet, Oxidation-Dependent Activation of Src Kinase Mediates Epithelial IL-33 Production and Signaling during Acute Airway Allergen Challenge. *J Immunol* **206**, 2989-2999 (2021); published online EpubJun 15 (10.4049/jimmunol.2000995).

53. B. M. Gumbiner, N.-G. Kim, The Hippo-YAP signaling pathway and contact inhibition of growth. *Journal of Cell Science* **127**, 709-717 (2014)10.1242/jcs.140103).

54. C. Blanchetot, M. l. J. Chagnon, N. Dubé, M. Hallé, M. L. Tremblay, Substrate-trapping techniques in the identification of cellular PTP targets. *Methods* **35 1**, 44-53 (2005).

55. F. Mercan, A. M. Bennett, Analysis of protein tyrosine phosphatases and substrates. *Curr Protoc Mol Biol* **Chapter 18**, Unit 18.16 (2010); published online EpubJul (10.1002/0471142727.mb1816s91).

56. Y. Han, Q. Gao, Y. Xu, K. Chen, R. Li, W. Guo, S. Wang, Cysteine sulfenylation contributes to liver fibrosis via the regulation of EphB2-mediated signaling. *Cell Death & Disease* **15**, 602 (2024); published online Epub2024/08/20 (10.1038/s41419-024-06997-9).

57. R. F. Queiroz, C. P. Stanley, K. Wolhuter, S. M. Y. Kong, R. Rajivan, N. McKinnon, G. T. H. Nguyen, A. Roveri, S. Guttzeit, P. Eaton, W. A. Donald, F. Ursini, C. C. Winterbourn, A. Ayer, R. Stocker, Hydrogen peroxide signaling via its transformation to a stereospecific alkyl hydroperoxide that escapes reductive inactivation. *Nature Communications* **12**, 6626 (2021); published online Epub2021/11/16 (10.1038/s41467-021-26991-5).

58. T. Senga, H. Hasegawa, M. Tanaka, M. A. Rahman, S. Ito, M. Hamaguchi, The cysteine-cluster motif of c-Src: Its role for the heavy metal-mediated activation of kinase. *Cancer Science* **99**, 571-575 (2008); published online Epub2008/03/01 (https://doi.org/10.1111/j.1349-7006.2007.00714.x).

59. A. E. van Vlimmeren, R. Voleti, C. A. Chartier, Z. Jiang, D. Karandur, P. A. Humphries, W. L. Lo, N. H. Shah, The pathogenic T42A mutation in SHP2 rewires the interaction specificity of its N-terminal regulatory domain. *bioRxiv*, (2024); published online EpubApr 9 (10.1101/2023.07.10.548257).

60. J. V. Evans, A. G. Ammer, J. E. Jett, C. A. Bolcato, J. C. Breaux, K. H. Martin, M. V. Culp, P. M. Gannett, S. A. Weed, Src binds cortactin through an SH2 domain cystine-mediated linkage. *Journal of cell science* **125**, 6185-6197 (2012); published online Epub2012/12// (10.1242/jcs.121046).

61. H. Xiao, M. P. Jedrychowski, D. K. Schweppe, E. L. Huttlin, Q. Yu, D. E. Heppner, J. Li, J. Long, E. L. Mills, J. Szpyt, Z. He, G. Du, R. Garrity, A. Reddy, L. P. Vaites, J. A. Paulo, T. Zhang, N. S. Gray, S. P. Gygi, E. T. Chouchani, A Quantitative Tissue-Specific Landscape of Protein Redox Regulation during Aging. *Cell* **180**, 968-983.e924 (2020); published online EpubMar 5 (10.1016/j.cell.2020.02.012).

62. Q. Yan, B. Tiago, V. P. R., D. Sebastian, K. T. A., W. Arthur, J. and Kuriyan, Structural Basis for Activation of ZAP-70 by Phosphorylation of the SH2-Kinase Linker. *Molecular and Cellular Biology* **33**, 2188-2201 (2013); published online Epub2013/06/01 (10.1128/MCB.01637-12).

63. D. Liu, D. Cowburn, Combining biophysical methods to analyze the disulfide bond in SH2 domain of C-terminal Src kinase. *Biophys Rep* **2**, 33-43 (2016)10.1007/s41048-016-0025-4).

1267 64. K. B. Kaplan, K. B. Bibbins, J. R. Swedlow, M. Arnaud, D. O. Morgan, H. E. Varmus,
1268 Association of the amino-terminal half of c-Src with focal adhesions alters their properties
1269 and is regulated by phosphorylation of tyrosine 527. *Embo j* **13**, 4745-4756 (1994); published
1270 online EpubOct 17 (10.1002/j.1460-2075.1994.tb06800.x).
1271 65. M. V. Hunter, P. M. Willoughby, A. E. E. Bruce, R. Fernandez-Gonzalez, Oxidative Stress
1272 Orchestrates Cell Polarity to Promote Embryonic Wound Healing. *Developmental Cell* **47**,
1273 377-387.e374 (2018)10.1016/j.devcel.2018.10.013).
1274 66. Y. Yang, X. Dong, S. Zheng, J. Sun, J. Ye, J. Chen, Y. Fang, B. Zhao, Z. Yin, P. Cao, L. Luo,
1275 GSTpi regulates VE-cadherin stabilization through promoting S-glutathionylation of Src.
1276 *Redox Biology* **30**, 101416 (2020); published online Epub2020/02/01/
1277 (https://doi.org/10.1016/j.redox.2019.101416).
1278 67. D. L. Wheeler, M. Iida, E. F. Dunn, The role of Src in solid tumors. *Oncologist* **14**, 667-678
1279 (2009); published online EpubJul (10.1634/theoncologist.2009-0009).
1280 68. C. Glorieux, S. Liu, D. Trachootham, P. Huang, Targeting ROS in cancer: rationale and
1281 strategies. *Nature Reviews Drug Discovery* **23**, 583-606 (2024); published online
1282 Epub2024/08/01 (10.1038/s41573-024-00979-4).
1283 69. S. Rao, D. Gurbani, G. Du, R. A. Everley, C. M. Browne, A. Chaikuad, L. Tan, M. Schröder,
1284 S. Gondi, S. B. Ficarro, T. Sim, N. D. Kim, M. J. Berberich, S. Knapp, J. A. Marto, K. D.
1285 Westover, P. K. Sorger, N. S. Gray, Leveraging Compound Promiscuity to Identify
1286 Targetable Cysteines within the Kinome. *Cell Chemical Biology* **26**, 818-829.e819 (2019);
1287 published online Epub2019/06/20/ (https://doi.org/10.1016/j.chembiol.2019.02.021).
1288 70. L. Boike, N. J. Henning, D. K. Nomura, Advances in covalent drug discovery. *Nature*
1289 *Reviews Drug Discovery* **21**, 881-898 (2022); published online Epub2022/12/01
1290 (10.1038/s41573-022-00542-z).
1291 71. J. Li, U. Rix, B. Fang, Y. Bai, A. Edwards, J. Colinge, K. L. Bennett, J. Gao, L. Song, S.
1292 Eschrich, G. Superti-Furga, J. Koomen, E. B. Haura, A chemical and phosphoproteomic
1293 characterization of dasatinib action in lung cancer. *Nature Chemical Biology* **6**, 291-299
1294 (2010); published online Epub2010/04/01 (10.1038/nchembio.332).
1295 72. E. Jurrus, D. Engel, K. Star, K. Monson, J. Brandi, L. E. Felberg, D. H. Brookes, L. Wilson, J.
1296 Chen, K. Liles, M. Chun, P. Li, D. W. Gohara, T. Dolinsky, R. Konecny, D. R. Koes, J. E.
1297 Nielsen, T. Head-Gordon, W. Geng, R. Krasny, G. W. Wei, M. J. Holst, J. A. McCammon, N.
1298 A. Baker, Improvements to the APBS biomolecular solvation software suite. *Protein Sci* **27**,
1299 112-128 (2018); published online EpubJan (10.1002/pro.3280).
1300 73. G. W. Fearnley, K. A. Young, J. R. Edgar, R. Antrobus, I. M. Hay, W. C. Liang, N. Martinez-
1301 Martin, W. Lin, J. E. Deane, H. J. Sharpe, The homophilic receptor PTPRK selectively
1302 dephosphorylates multiple junctional regulators to promote cell-cell adhesion. *Elife* **8**,
1303 (2019); published online EpubMar 29 (10.7554/eLife.44597).
1304 74. I. M. Hay, G. W. Fearnley, P. Rios, M. Köhn, H. J. Sharpe, J. E. Deane, The receptor PTPRU
1305 is a redox sensitive pseudophosphatase. *Nature Communications* **11**, 3219 (2020); published
1306 online Epub2020/06/26 (10.1038/s41467-020-17076-w).
1307 75. D. P. Byrne, S. Shrestha, M. Galler, M. Cao, L. A. Daly, A. E. Campbell, C. E. Eyers, E. A.
1308 Veal, N. Kannan, P. A. Eyers, Aurora A regulation by reversible cysteine oxidation reveals
1309 evolutionarily conserved redox control of Ser/Thr protein kinase activity. *Sci Signal* **13**,
1310 (2020); published online EpubJul 7 (10.1126/scisignal.aax2713).
1311 76. K. Wojdyla, A. Rogowska-Wrzesinska, Differential alkylation-based redox proteomics –
1312 Lessons learnt. *Redox Biology* **6**, 240-252 (2015); published online Epub2015/12/01/
1313 (https://doi.org/10.1016/j.redox.2015.08.005).
1314 77. S. Ferries, S. Perkins, P. J. Brownridge, A. E. Campbell, P. A. Eyers, A. R. Jones, C. E.
1315 Eyers, Evaluation of Parameters for Confident Phosphorylation Site Localization Using an
1316 Orbitrap Fusion Tribrid Mass Spectrometer. *Journal of proteome research* **16 9**, 3448-3459
1317 (2017).
1318 78. L. A. Daly, D. P. Byrne, S. Perkins, P. J. Brownridge, E. McDonnell, A. R. Jones, P. A.
1319 Eyers, C. E. Eyers, Custom Workflow for the Confident Identification of Sulfotyrosine-
1320 Containing Peptides and Their Discrimination from Phosphopeptides. *J Proteome Res* **22**,
1321 3754-3772 (2023); published online EpubDec 1 (10.1021/acs.jproteome.3c00425).

79. S. Ferries, S. Perkins, P. J. Brownridge, A. Campbell, P. A. Eyers, A. R. Jones, C. E. Eyers, Evaluation of Parameters for Confident Phosphorylation Site Localization Using an Orbitrap Fusion Tribrid Mass Spectrometer. *J Proteome Res* **16**, 3448-3459 (2017); published online EpubSep 1 (10.1021/acs.jproteome.7b00337).
80. D. N. Perkins, D. J. Pappin, D. M. Creasy, J. S. Cottrell, Probability-based protein identification by searching sequence databases using mass spectrometry data. *Electrophoresis* **20**, 3551-3567 (1999); published online EpubDec (10.1002/(sici)1522-2683(19991201)20:18<3551::Aid-elps3551>3.0.Co;2-2).
81. J. C. Silva, M. V. Gorenstein, G. Z. Li, J. P. Vissers, S. J. Geromanos, Absolute quantification of proteins by LCMSE: a virtue of parallel MS acquisition. *Mol Cell Proteomics* **5**, 144-156 (2006); published online EpubJan (10.1074/mcp.M500230-MCP200).
82. James M. Murphy, Q. Zhang, Samuel N. Young, Michael L. Reese, Fiona P. Bailey, Patrick A. Eyers, D. Ungureanu, H. Hammaren, O. Silvennoinen, Leila N. Varghese, K. Chen, A. Tripaydonis, N. Jura, K. Fukuda, J. Qin, Z. Nimchuk, Mary B. Mudgett, S. Elowe, Christine L. Gee, L. Liu, Roger J. Daly, G. Manning, Jeffrey J. Babon, Isabelle S. Lucet, A robust methodology to subclassify pseudokinases based on their nucleotide-binding properties. *Biochemical Journal* **457**, 323-334 (2013)10.1042/BJ20131174).
83. F. Madeira, N. Madhusoodanan, J. Lee, A. Eusebi, A. Niewielska, A. R. N. Tivey, R. Lopez, S. Butcher, The EMBL-EBI Job Dispatcher sequence analysis tools framework in 2024. *Nucleic Acids Res* **52**, W521-W525 (2024); published online Epub2024/07// (10.1093/nar/gkae241).
84. A. M. Waterhouse, J. B. Procter, D. M. A. Martin, M. Clamp, G. J. Barton, Jalview Version 2—a multiple sequence alignment editor and analysis workbench. *Bioinformatics* **25**, 1189-1191 (2009)10.1093/bioinformatics/btp033).
85. D. Bajusz, G. Pándy-Szekeres, Á. Takács, E. D. de Araujo, G. M. Keserű, SH2db, an information system for the SH2 domain. *Nucleic Acids Res* **51**, W542-W552 (2023)10.1093/nar/gkad420).

Acknowledgements: We thank the Babraham Institute imaging facility, J. Clark in the Babraham Institute biological chemistry facility, C. Switzer for discussions about redox chemistry, T. Chessa for advice on retroviral transduction, K. Wojdyla for advice on differential alkylation, and E. Veal, P. Hawkins, A. Tuncay, R. Williams and members of the Sharpe lab for critical feedback on the manuscript. **Funding:** This work was supported by a Sir Henry Dale Fellowship jointly funded by the Wellcome Trust and the Royal Society [109407/A/15/A] awarded to HJS, an ESPRC Frontier guarantee grant [EP/Z000114/1], a BBSRC institutional programme grant [BBS/E/B/000C0433] and core capability grant [BB/CCG2210/1]. OR is supported by a studentship funded by the Lister Institute of Preventive Medicine. MB in the Roger Williams group is supported by the Medical Research Council (MC_U105184308 to RLW) and Cancer Research UK (grant DRCPGM\100014 to RLW). PC and NC were supported by Cancer Research UK grants C9685/A26398, C9685/A27415, and C9545/A29580. JM and DE are being supported by a VIB grant. LAD/DPB/CEE and PAE acknowledge UKRI equipment and project funding through BBSRC grants BB/S018514/1 BB/R000182/1 and BB/X002780/1. HJS is an EMBO Young Investigator and Lister Institute Prize Fellow. **Author contributions:** Conceptualization: KEM, DPB, HJS. Methodology: KEM, MB, NC, OR, DE, LAD, SAC, DPB. Investigation: KEM, NC, OR, DE, DPB. Formal analysis: KEM, MB, NC, OR, DE, LAD, SAC, DPB. Visualization: KEM, MB, NC, OR, DE, TL, SAC, DPB, HJS. Validation: KEM, DPB. Data curation: HEJ, HJS. Funding acquisition: PC, CEE, JM, PAE, HJS. Project Administration: HJS. Supervision: PC, CEE, JM, PAE, HJS. Resources: PC, CEE, JM, PAE, HJS. Writing – original draft: KEM, DPB, HJS. Writing – review and editing: KEM, MB, NC, CEE, JM, PAE, DPB, HJS. **Competing interests:** The authors

declare that they have no competing interests. **Data and materials availability:** Mass spectrometry data have been deposited to the ProteomeXchange Consortium through the PRIDE partner repository with the dataset identifiers PXD059503 (CPT enrichment), PXD059641(Cysteine S-sulfonate modifications) and PXD059840 (HDX-MS). All other materials are available upon request to the corresponding authors.

Figure legends

Fig. 1. PV perturbs redox homeostasis and induces tyrosine phosphorylation in SRC dependent manner.

(A) Schematic of mono-peroxo and di-peroxo-vanadium (PV compounds) generated using ChemDraw. **(B)** HEK293T cells were treated as shown, lysed and subjected to immunoblot analysis using the indicated antibodies. Image representative of N=3 experiments. (**C**) Representative false colour images of F488/405 ratio (scaled 1-9) from **movies S1 and S2** of U2OS cells stably expressing plasma membrane (PM) localised HyPer7 and treated with 100 μM PV or media. Scale bar = 20 μm. (**D**) Quantification of the ratio of the two excitation maxima (F488/405), normalized against initial value, of PM-HyPer7 expressing U2OS cells over a time course, imaged every 20 s. Treatments were added at 60 s (arrow). Mean of n=3 ± SD plotted. ** $p \leq 0.001$ Unpaired t-test at t= 400 s. (**E**) Ratio of the two excitation maxima (F500/400) of recombinantly expressed HyPer7 (2.5 μM) following its treatment with the indicated reagents. The bars represent the mean of n=3 ± SD. *** $p \leq 0.001$; ns – non-significant. The p-value is based on Dunnett's multiple comparisons test of a one-way ANOVA. (**F**) Quantification of the ratio of the two excitation maxima (F488/405), normalized against initial value, of PM-HyPer7 expressing U2OS cells over a time course, imaged every 20 s. Treatments were added at 60 s (arrow). Mean of n=3 ± SD plotted. (**G**) Cells were subjected to the indicated PV time course, washed with PBS with catalase and NEM, prior to lysis without NEM. Samples were resolved on non-reducing or reducing gels as indicated to distinguish PRDX1 monomers from disulfide-linked dimers. Total and phospho PRDX1 blots are from separate gels but the same samples. Representative of n=3 experiments. (**H**) Densitometric quantification of PRDX1 dimer and monomer bands from G. Mean of n=3 ± SD plotted. (**I**) HEK293T cells were treated with the indicated tyrosine kinase inhibitors at IC_{50} (+) and 2.5x IC_{50} (‡) concentrations for 2 h prior to addition of 100 μM PV for 15 min before lysis and immunoblotting with annotated antibodies. (**J**) Dasatinib targets based on (*71*) and mapped onto the tyrosine kinase arm of the Human kinome using kinmap (http://kinhub.org/kinmap/). (**K**) WT and Src/Yes/Fyn (SYF) WT and KO cells were stimulated with 100 μM PV for the indicated times prior to lysis and immunoblotting with indicated antibodies. Red arrow indicates 130 kDa. Representative of 3 experiments.

See also Figs. S1-S3.

Fig. 2. SRC is oxidized on specific cysteines and activated by PV.

(**A**) 6xHis-SRC (3 ng) dependent phosphorylation of a specific fluorescent substrate (2 μM). Data shown is relative SRC activity in the presence of the indicated concentrations of PV compared to a buffer only control. SRC was preincubated for 0, 10, 60 or 120 mins prior to initiation of the kinase assay. Means ± SD n=3 experiments are shown. (**B**) Dose response curve for H_2O_2 pre-incubated with recombinant 6xHis-SRC (3 ng) for the indicated time periods. Reactions were initiated with the addition of peptide substrate and ATP, and phosphorylation was measured after 15- and 25-mins assay time. Data shown is relative SRC activity in the presence of the indicated concentrations of H_2O_2 compared to a buffer only control. Means of n=3 ± SD shown. (**C**) HEK293T cells treated with the indicated

1421 concentrations of PV for 15 min, were lysed in catalase and NEM-containing buffer. Reversibly
1422 oxidised thiols were reduced with TCEP, and newly regenerated thiol(ate)s were labelled with
1423 Iodoacetyl-PEG2-Biotin. Lysates and biotinylated proteins were then affinity purified using
1424 streptavidin beads and subjected to immunoblotting with indicated antibodies. Blot
1425 representative of 3 experiments. (**D**) HEK293T cells transiently expressing StrepII-tag fused
1426 SRC were treated as indicated, and SRC affinity purified by streptactin pull down. Purified
1427 protein was then subjected to tryptic digest and analysed by LC/MS-MS for triply oxidised
1428 cysteine (sulphonic acid). (**E**) SRC isolated from transfected HEK293T cells by streptactin
1429 affinity purification was incubated with or without 5 mM PV, followed by tryptic digest and
1430 analysis by LC MS/MS. Values are normalized against abundance of non-cysteine containing
1431 SRC peptides. (**F**) Schematic of SRC kinase indicating the position of two key regulatory
1432 phosphosites (Circle with P) as well as the two most readily oxidixed cysteine residues (red
1433 stars). (**G**) Surface electrostatic potential (*72*) for regions surrounding Cys 280 (PDB:2SRC)
1434 and Cys 188 and Cys241 (PDB:1Y57). Units = K_bT/e_c. (**H**) Phosphorylation of the fluorescent
1435 peptide substrate by WT (black), C188A (blue) and C280A (red) SRC isolated from HEK293T
1436 cells by streptactin affinity purification was measured after 30 min. Means of n=3 ± SD are
1437 shown. (**I**) Dose-response curves for PV. WT (black), C188A (blue) and C280A (red) SRC
1438 isolated from HEK-293T cells by streptactin affinity purification and incubated with the
1439 indicated concentrations of PV for 10 mins. Phosphorylation of the fluorescent peptide
1440 substrate was measured after 15 min. Data shown is % SRC activity compared to a buffer
1441 control. Means of n=3 ±SD are shown. FL = full-length. (**J**) SYF KO MEFs were retrovirally-
1442 transduced with specified SRC expression constructs and treated with PV as shown, before
1443 lysis and immunoblotting with indicated antibodies. Red arrow indicates relevant band.
1444 Representative of >3 experiments. (**K**) Densitometric quantification of western blot in Fig. 2J.
1445 Ratios of phosphorylated cortactin/total tubulin levels are shown.
1446
1447 See also Fig. S3.
1448
1449 **Fig. 3. PV induces specific conformational changes in SRC.**
1450 **(A, B**) HDX-MS analysis of pervanadate treated SRC. Relative fractional uptake (RFU)
1451 differences between 5 μM SRC and SRC incubated with 0.5 mM (**A**) and 2.5 mM (**B**) PV were
1452 mapped on the closed (Left) and the open conformations (Right) of SRC (PDB: 2SRC and
1453 1Y57, respectively). Regions showing significant protection and becoming less solvent
1454 exposed are colored in blue and regions showing significant deprotection and becoming more
1455 solvent exposed are presented in red. Regions where no significant differences were observed
1456 are shown in white, while grey denotes parts of SRC for which no peptides were observed.
1457 Key cysteines are highlighted in purple and key phosphorylation sites are highlighted in light
1458 blue. The overall coverages were 80% and 60% for the 0.5 mM and 2.5 mM PV HDX-MS
1459 experiments, respectively.
1460
1461 See also Fig. S4.
1462
1463 **Fig. 4**. **Cys 188 oxidation or mutation impacts SRC-SH2 phosphopeptide binding.**
1464 **(A**) SRC-SH2 with highlighted regions protected (blue) and deprotected (red) from deuterium
1465 exchange upon 0.5 mM PV treatment (PDB:2SRC) based on data from Fig. 3. (**B**) Alphafold3
1466 (*42*) model of SRC $SH2^{WT}$ bound to the phosphorylated SRC C-terminal peptide:
1467 FTSTEPQpYQPGENL. ipTM = 0.73. (**C**) Residues predicted to form hydrogen bonds (blue
1468 dashed lines) based on AF3 models. Top: As in B. Middle: AF3 model with SRC s-nitroso

1469 cysteine 188 and C terminal peptide. ipTM = 0.75. Bottom: AF3 model with C188A and C
1470 terminal peptide. ipTM = 0.72. (**D**) Isothermal titration calorimetry (ITC) titration curves of the
1471 interaction between SRC-SH2 and indicated phosphopeptides. The SH2 domain was
1472 pretreated with 1 mM TCEP or 0.1 mM PV prior to the assay. Upper: baseline-corrected
1473 differential power plotted over time. Lower: normalized binding curve showing the integrated
1474 change in enthalpy against the molar ratio. Stoichiometry (N), mean enthalpy change (ΔH)
1475 and mean K_D ±SD shown based on n =3 assays. (**E**) AF3 model of hydrogen bonding network
1476 between residues within the JAK1 SH2 domain engaging glutamate on IFNR1. ipTM = 0.69.
1477
1478 See also Fig. S5.
1479
1480 **Fig. 5. SRC cysteines are required to overcome contact inhibition**
1481 (**A**) SYF KO MEFs were retrovirally transduced with specified SRC expression constructs and
1482 treated with 100 μM PV as shown, before lysis and immunoblotting with indicated antibodies.
1483 (**B**) Cell numbers were determined over time in culture for SYF KO MEFs, retrovirally
1484 transduced with specified SRC expression constructs (as in A). (**C**) Confocal microscopy
1485 images of SYF KO MEFs complemented with the indicated constructs grown to post-
1486 confluence, fixed, permeabilized and stained with the DAPI (nuclei; blue) and Phalloidin (actin;
1487 red). (**D**) Quantification of nuclei taken from 5 or 6 fields of view per cell line. **** p.Adj < 0.001.
1488 Ordinary one-way ANOVA with Tukey's correction for multiple comparisons. (**E**) SYF KO
1489 MEFs expressing the indicated constructs were grown to post-confluence, lysed and
1490 immunoblotted with the indicated antibodies. Representative blot from n=3 experiments. (**F**)
1491 In summary, Pervanadate induces numerous cellular changes. Increases in pTyr can be
1492 attributed to the hyperoxidation of PTP catalytic cysteines as well as direct oxidation of specific
1493 cysteines on SRC and YES leading to relief of autoinhibition and activation. Furthermore, PV
1494 induces rapid oxidation of HyPer7, a reporter for both H2O2 and the activity of cellular
1495 antioxidant systems such as thioredoxin and glutaredoxin. PV therefore disrupts redox
1496 homeostasis in addition to increasing phosphotyrosine levels.
1497
1498 See also Fig. S6.
1499